The anharmonic infrared spectra of polycyclic aromatic hydrocarbons

Mackie, J.C.

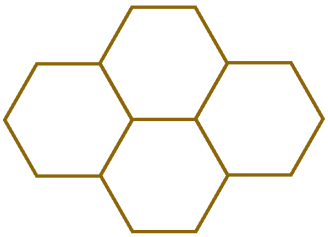

The anharmonic quartic force field infrared spectra of five non-linear Polycyclic Aromatic Hydrocarbons: benzanthracene, chrysene, phenanthrene, pyrene, and triphenylene

The study of interstellar polycyclic aromatic hydrocarbons (PAHs) relies heavily on theoretically predicted infrared (IR) spectra. Most earlier studies use scaled harmonic frequencies for band positions and the double harmonic approximation for intensities. However, recent high–resolution gas–phase experimental spectroscopic studies have shown that the harmonic approximation is not sufficient to reproduce experimental results. In our previous work we presented the anharmonic theoretical spectra of three linear PAHs, showing the importance of including anharmonicities into the theoretical calculations. In this paper, we continue this work by extending the study to include five non–linear PAHs (benz[a]anthracene, chrysene, phenanthrene, pyrene, and triphenylene), thereby allowing us to make a full assessment of how edge structure, symmetry and size influence the effects of anharmonicities. The theoretical anharmonic spectra are compared to spectra obtained under matrix isolation low–temperature conditions, low–resolution high–temperature gas–phase conditions, and high–resolution low–temperature gas–phase conditions. Overall, excellent agreement is observed between the theoretical and experimental spectra although the experimental spectra show subtle but significant differences.

C. J. Mackie, A. Candian, X. Huang, E. Maltseva, A. Petrignani, J. Oomens, A. L. Mattioda, W. J. Buma, T. J. Lee, and A. G. G. M. Tielens, J. Chem. Phys **145**, 084313 (2016)

4.1 Introduction

Polycyclic Aromatic Hydrocarbons (PAHs) are a family of molecules characterized by fused aromatic–benzenoid rings with the free carbon edges capped by hydrogens. These molecules are of great interest in a wide variety of scientific fields. From a material science standpoint they serve as models and precursors for various carbon–based nano–materials such as nanotubes, graphene, and fullerenes[5, 6, 7]. From an engineering standpoint they are a common, yet undesirable, by–product of combustion in engines and rockets[1, 2]. From a biological standpoint they are viewed as a common pollutant and are studied in the context of their carcinogenic properties[3].

PAHs are also of interest from the astrophysical standpoint. They are the most likely candidate for a set of infrared (IR) features known as the Aromatic Infrared Bands (AIBs)[29, 30] observed around a wide variety of astronomical objects. It has been estimated that up to 20% of the total carbon in the universe is locked up in PAHs[78]. Their importance has led experimentalists, theoreticians, and astronomers to work closely in order to characterize the IR emission of PAHs for use as a probe of the physical and chemical conditions in the astrophysical environments in which they are observed.

Experimental IR spectra have been reported for a wide variety of PAHs using various spectroscopic techniques. Due to the involatile nature of PAHs two dominant techniques are used to obtain the IR spectrum: high–temperature gas–phase spectroscopy, or low–temperature matrix–isolation spectroscopy[21, 22, 23, 24, 79, 80, 81, 82]. Attempts to extrapolate these experimental data to astrophysically relevant conditions are complicated by temperature effects in the former, and matrix–interaction effects in the latter. High–resolution low–temperature gas–phase spectra have been taken previously, but only for a handful of species and only in the C–H stretching region (2950–3150 cm^{-1}, 3μm)[25, 104].

The limited availability of PAH absorption spectra of the sizes and structures relevant to astrophysical environments has necessitated the development and use of computational quantum chemical techniques for PAHs. Databases of the IR spectra of astrophysically relevant PAHs have been compiled and are available online[36, 50]. Typically these theoretical IR spectra are constructed using the harmonic approximation within the Density Functional Theory (DFT) framework using B3LYP functionals with very small basis sets (e.g., 4–31G). This approach has been successful in roughly reproducing the overall IR features, but has compared poorly to high–resolution experiments[25]. Specifically the C–H stretching region and the pure combination band region (1700–2000 cm^{-1}) are incorrectly reproduced since mode couplings, resonances, and combination bands cannot be modelled at the harmonic level.

It has been shown in our previous work[25, 105] that an anharmonic theoretical approach is necessary to explain the experimental IR spectra of PAHs. While previous work concentrated on a set of three linear PAHs, this work expands to include a set of five non–linear PAHs which complete the series of PAHs containing up to four benzenoid rings. The reason for this choice is twofold; we want to show that the anharmonic treatment can be extended successfully to non-linear species, and at

the same time we want to understand how edge structure and symmetry influence the anharmonic spectrum. In fact, variations in the IR spectra of PAHs have been observed experimentally and have been attributed to various hydrogen–hydrogen interaction edge effects[106, 107], and to the variation in molecular symmetries from species to species. To study these edge and symmetry effects non–linear PAHs must be considered. This work aims to show that the anharmonic treatment can be extended to non–linear species: benz[a]anthracene ($C_{18}H_{12}$), chrysene ($C_{18}H_{12}$), phenanthrene ($C_{14}H_{10}$), pyrene ($C_{16}H_{10}$), and triphenylene ($C_{18}H_{12}$) (fig. 5.1). Moreover, we present low–temperature high–resolution gas–phase experimental IR absorption spectra of the five non–linear PAHs (first presented in the astrophysical companion paper[26]), as well as matrix–isolation spectra (MIS) which allows for direct comparisons with theory providing further validation for our approach. Although the theoretical spectra produced is in absorption at 0 K, understanding the fundamental nature of the anharmonicity of PAHs and the importance of resonances will allow us to better understand the emission features of astronomical PAHs.

4.2 Theory

The most commonly applied approximation in predicting the IR absorption characteristics of a molecule is the assumption of harmonic potentials. Given the equilibrium structure of a molecule, the nuclear potential can be approximated with just the second-order terms in a Taylor series expansion, referred to as the quadratic force constants. Solving for the eigenvectors and eigenvalues of this system of quadratic force constants leads to the normal mode atomic displacement descriptions and the excitation energies of each mode. The IR intensities of the modes are then calculated by what is called the double–harmonic approximation, which involves taking the derivative of the dipole of the molecule as it is displaced along the normal modes. The harmonic (and double-harmonic) approximation only allows the vibrational fundamentals to exhibit any IR intensity, and can greatly overestimate the energies of the fundamentals due to the neglect of anharmonicity.

In order to produce a more realistic spectrum, additional terms need to be included when producing the vibrational potential (and the dipole surface). This is accomplished through an anharmonic quartic force field (QFF) and consequential vibrational analysis. In this case, the nuclear potential is expanded to include up to quartic terms in the Taylor series expansion. Since the potential is no longer quadratic, an analytic solution for the modes and energies is no longer possible (as is possible for the harmonic case). As such, second–order vibrational perturbation theory (VPT2) is required to solve for the energies. The introduction of VPT2, however, leads to the possibility of singularities (near–zero terms in denominators if two states are very close in energy). The terms wherein singularities arise are removed from the VPT2 formula, and instead a matrix is constructed, including diagonal and coupling terms, that is then diagonalized. Four types of resonances are considered: Fermi one (a fundamental is approximately equal to an overtone),

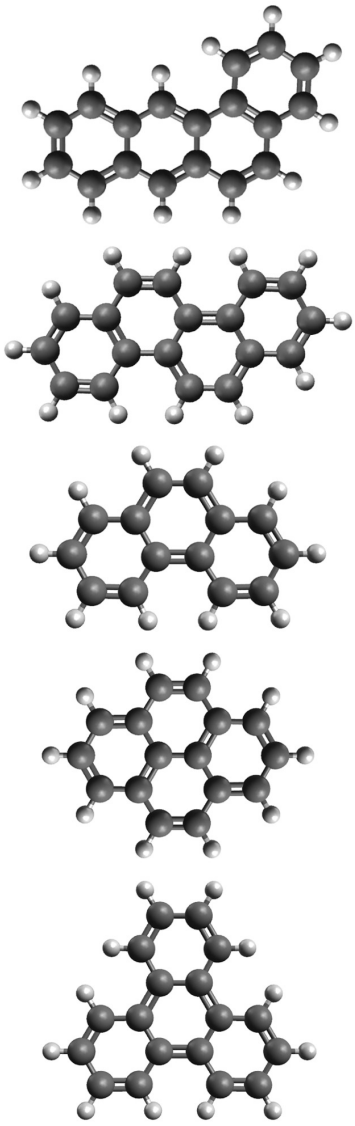

Figure 4.1 From top to bottom: benz[a]anthracene, chrysene, phenanthrene, pyrene, and triphenylene.

Fermi two (a fundamental is approximately equal to a combination band), Darling-Dennison (two overtones or two combination bands or a mixture of these two are approximately equal), and Coriolis (two fundamentals are approximately equal). The effect of a resonance is to push one member of the pair of states to a lower energy and the other to a higher energy. Intensity sharing across a resonance also occurs, which can result in bands that would normally be of zero or minimal intensity to gain significant intensity.

Additional complications arise when multiple modes or combination bands are in simultaneous resonances, respectively. These so–called *polyads*, need to be considered together through a resonance matrix (see Ref.58), and is the source of the vibrational Darling-Dennison and Coriolis resonances. The resulting eigenvectors (squared) and eigenvalues of the resonance matrix give the percent mixing of individual modes and combination bands involved in the polyad, and the new energies arising from the multiple interactions. The intensities can also be calculated individually through anharmonic means, as described in Ref. [90]. However, when there are resonances, the anharmonic IR intensities will also have resonant terms that need to be removed. In our previous work it was shown that double harmonic intensities distributed according to the eigenvectors of the polyad matrix accurately reproduce intensity patterns[105]. For a more detailed description of the theory involved in this work see ref. 105 and references therein.

4.3 Methods

4.3.1 Theoretical Methods

The quantum chemical calculations in this work were performed with Gaussian 09[53] and the VPT2 calculations were performed with SPECTRO[54]. Gaussian was used to compute the optimized geometry of the molecules, the harmonic intensities, the anharmonic intensities (no polyad mixings), and the quartic force fields (quadratic, cubic, and quartic force constants). A DFT framework, with the B971 functional[93] and a T2ZP basis[94] was used for the Gaussian calculations, as suggested in refs. 95, 96.

Gaussian09 is able to compute the VPT2 anharmonic spectrum of molecules, however, it was unable to reproduce accurately the C–H stretching region of PAHs due to the large number of simultaneous resonances occurring[25]. Therefore, the SPECTRO program was used to carry out the VPT2 calculations in order to handle these large resonant groups, or *polyads*.

The optimized geometry and the normal coordinate QFF of each molecule was taken from the Gaussian output and input into SPECTRO. Since the current version of SPECTRO cannot take normal coordinate QFFs as input, a linear transformation into Cartesian coordinates[97] was performed first.

SPECTRO determines what are considered to be resonant states, and therefore must be removed from the regular VPT2 treatment, through a set of thresholds. Two types of threshold are present: the maximum energy separation of the states considered Δ (denominator term), and the interaction strength of the states W (numerator term). In our previous work[105] it was found that the default values

used by SPECTRO to detect resonances ($\Delta = 200$ cm^{-1} and $W = 10$ cm^{-1}) were sufficient, i.e., the spectrum did not change significantly as these thresholds were further increased. After testing it was determined that the W threshold was allowing singularities (missed resonances) to enter into the VPT2 treatment causing significant changes to the resulting spectrum. As such, the W threshold was set to zero and resonances were detected purely on the energy separation of the states. A side effect of this however, is that it allows for states with incorrect symmetry to enter into resonance unnecessarily. A separate subroutine was therefore written to ensure symmetry constraints were obeyed. In passing by, we notice that if these symmetry constraints are broken, it will not cause changes to the computed spectrum, but it would increase significantly the number of resonant states and thus polyad sizes. This results in an unnecessary increase in computational time by adding many zero–valued entries to the resonance matrices.

The final QFF anharmonic spectra were constructed using the line positions from SPECTRO, the anharmonic intensities from Gaussian (for modes not in polyads), and the harmonic intensities from Gaussian distributed across the polyads (for modes in polyads), as described in Ref. [105].

Special theoretical consideration is necessary for triphenylene since it is a symmetric top with $\mathcal{D}_{3h}$ symmetry; additional discussion is given in the appendix.

4.3.2 Experimental Methods (MIS)

The MIS IR spectroscopic techniques employed for these samples have been described in detail elsewhere [79, 108, 109] and will only be briefly summarized here. All samples were isolated in an inert argon matrix prepared by vapor co–deposition of the PAH of interest with an over abundance of argon (Ar) onto a 15K CsI window suspended in a high–vacuum chamber (p $<10^{-8}$ Torr). The sample being investigated was vaporized from a heated Pyrex tube while the argon (Matheson prepurified, 99.998%) was admitted through an adjacent length of liquid nitrogen cooled copper tubing, to minimize water and other contaminates. The conditions were optimized to produce an Ar/PAH ratio in excess of ≈1000:1. An FTIR spectrum of the sample was recorded once a sufficient amount of neutral material was accumulated, as indicated by the strength of the weakest bands.

Samples of chrysene ($C_{18}H_{12}$, 98% purity), pyrene ($C_{16}H_{18}$, 99% purity), phenanthrene ($C_{14}H_{10}$, 98% purity), and triphenylene ($C_{18}H_{12}$, 98% nominal purity) were obtained from the Aldrich Chemical Company. Significant impurities were noticed, initially, in the samples of triphenylene. These less volatile impurities were removed by baking out the sample, under vacuum, just below the sublimation temperature of the sample. The benz[a]anthracene (1,2-benzanthracene) sample was obtained from Resolutions Systems, the U.S. supplier for Chiron Chemical Company and was 99% or greater purity. Deposition temperatures for the PAHs discussed here were phenanthrene, 13^{o}C (cooled); pyrene, 65^{o}C; benz[a]anthracene, 85^{o}C; chrysene, 95^{o}C; and triphenylene, 85^{o}C. The mid–IR spectra for chrysene, pyrene, phenanthrene, and triphenylene were recorded on a Nicolet Analytical Instruments, Model 740 FTIR spectrometer using an MCT–B detector/KBr beam splitter combination while the benz[a]anthracene data was

collected on a Bio–Rad/Digilab Excalibur FTS–4000 IR spectrometer using an MCT–B detector/KBR broadband beam splitter combination. All spectra were recorded as a co–addition of either 250 or 500 scans at a resolution of 0.5 cm^{-1}. For presentation purposes, the reported spectra have been baseline-corrected with several bands resulting from impurities (such as water and purge air) either subtracted or truncated using the Win–IR Pro 3.4 Software package.

4.3.3 Experimental Methods (High–resolution Gas–phase)

The experimental setup used to perform laser spectroscopy on a supersonic molecular jet has been described previously[98] as well. A given sample was kept at a temperature higher than its melting point to create enough vapor pressure for detection. Mixed with 2 bars of a carrier gas (argon), the sample was expanded into the vacuum through a pulsed valve (General Valve) with a typical opening time of 200 μs.

Detection of the molecules after the expansion was achieved through resonance enhanced multiphoton ionization followed by mass-selective ion detection. A dye laser (Sirah Cobra Stretch) was fixed on a specific electronic transition of the molecule under investigation (see ref. 26 for more details) while an ArF excimer laser beam (Neweks PSX-501) in temporal overlap with the dye laser was used to ionize the molecules from the electronically excited state.

To probe the ground state vibrational levels an IR laser beam with a line width of 0.07 cm^{-1} was introduced 200 ns before the excitation and ionization beams. The 3 μm pulse was a product of difference frequency mixing of the fundamental outputs of the dye laser (Sirah Precision Scan with LDS798 dye) and the Nd:YAG laser (Spectra Physics Lab 190) in a $LiNbO_3$ crystal. Resonant excitation of vibrational levels resulted in depletion of ground state population of the probed molecules and thus led to a dip in the ion signal.

4.4 Results

In the following we will compare the theoretical anharmonic spectra with experimental spectra obtained under three different experimental conditions. To allow for a proper comparison, we have convolved the theoretical stick spectra with Lorentzian profiles with appropriate full-width half-maximums (FWHM) (2 cm^{-1} for the MIS spectra , 18 cm^{-1} for the high–temperature gas–phase spectra and 2 cm^{-1} for the high-resolution low–temperature gas–phase data). Figures 4.7 and 4.12 show visual comparisons between the convolved theoretical spectrum and the MIS experiment, high–temperature experiment, and the high-resolution low–temperature gas–phase experiment for benz[a]anthracene. See the supplemental material for similar comparisons of each PAH.

These sets of convolved theoretical spectra are then used to assign the best match between experimental and theoretical bands based on position, intensities, and overall feature trends. The values given for the experimental and convolved theoretical band positions and intensities were determined by fitting Lorentzian profiles to the spectra using the software package Fityk[110]. Experimental bands

with relative peak intensities under 1% of the maximum intensity bands have been excluded.

For the high–temperature gas–phase spectra, as well as the MIS, line position and intensity comparisons between experiment and theory are given in the supplemental material. Similar spectral features (i.e., position, intensities, and profiles) between the five species are aligned across the rows of the tables. The MIS spectra are of high enough resolution to warrant direct comparison of the vibrational modes types. It is important to note that vibrational mode descriptions become vague when describing modes that are in resonance; as such the spectral bands are organized by their dominant resonant component. Two strong water bands at 1608 cm^{-1} and 1624 cm^{-1} are observed in the MIS spectra for each PAH (and have been truncated), as well as a continuum–like feature under these water bands for chrysene and phenanthrene. Seven MIS bands could not be assigned with theoretical bands.

Individual bands are not resolved in the C–H stretching region of the high–temperature and MIS experiments due to temperature effects for the former, and steric hindrance of the hydrogens for the latter. Therefore, analysis of the C–H stretching region is performed only for the high–resolution gas–phase spectra. A detailed line assignment and comparison between theory and the high–resolution experiment is given for benz[a]anthracene in table 4.7 and mode descriptions in table , similar comparisons are available for each of the molecules in the supplemental material. Since resonance mixing between modes is so strong in this region assignment of each band to a fundamental or combination band is impossible. Instead only the dominant resonant components (typically components that are over 10% mixed) and dominant intensity sources can be identified (note that these intensity sources are not necessarily the dominant resonant sources). Along with these identifications, an ID letter is given for each band which corresponds with the identification letters in the respective spectra shown.

4.5 Discussion

4.5.1 MIS

Excellent agreement between the MIS spectra and the convolved anharmonic spectra was achieved. See the supplemental material for figures of the theoretical spectra compared to experiment, as well as tables listing the band positions, relative intensities, and mode descriptions. Broadening of the C–H stretching modes due to solid state interactions between the PAH and the matrix prevents meaningful comparison in this region. Comparison between theory and experiment for the C–H modes is therefore reserved for the high–resolution gas–phase experiments.

The average absolute percent differences in line positions between the MIS spectra and the convolved theoretical spectra are given in table 4.3 for each molecule. Figure 5.5 shows a histogram of the percent differences between the line positions of the theory and MIS for all five species combined. This leads to a Gaussian distribution with the average deviation being 0.41% ±0.63%. Previous work [111] has shown that argon matrix interaction effects lead to an average deviation

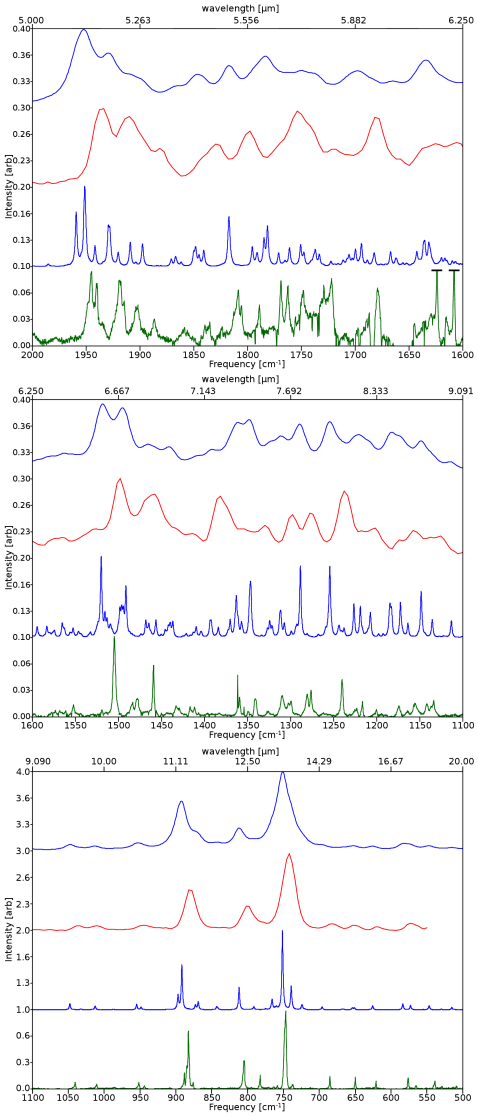

Figure 4.2 Comparison of the IR spectrum of benz[a]anthracene between the matrix–isolation experimental at 15 K (green, bottom spectrum of each panel), the theoretical anharmonic (this work) convolved with a FWHM of 2 cm^{-1} (blue, bottom middle spectrum of each panel), the gas–phase experimental at 300 K[21] (red, top middle spectrum of each panel), and the theoretical anharmonic (this work) convolved with a FWHM of 18 cm^{-1} (blue, top spectrum of each panel). Three spectral ranges are shown. Each range has its intensities normalized to the local maximum to enhance details. Water contaminant line intensities have been truncated.

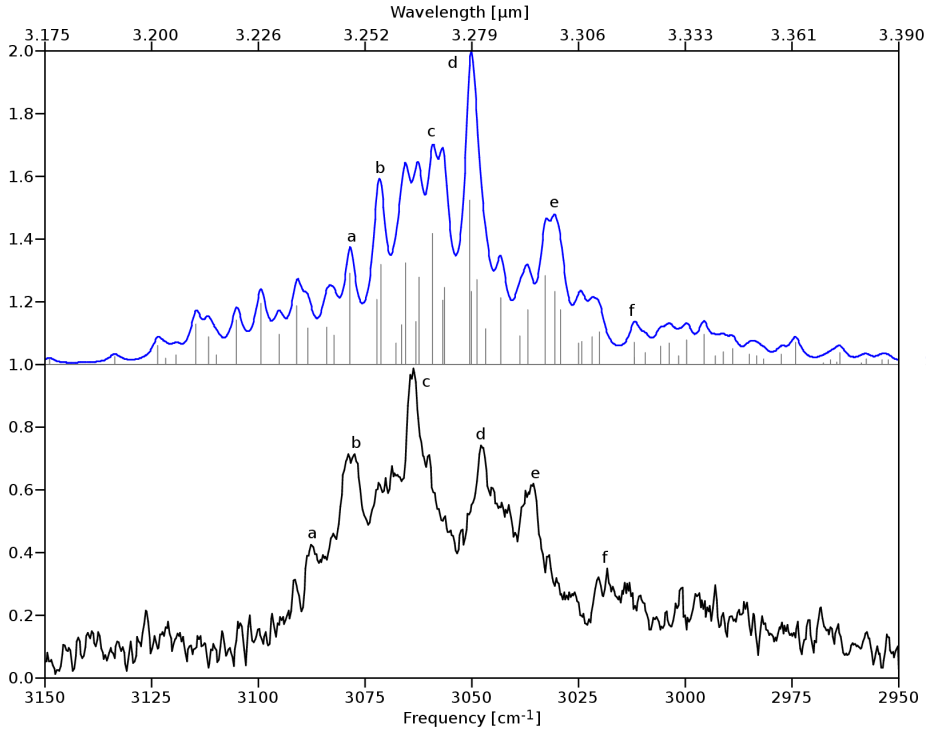

Figure 4.3 Anharmonic QFF IR spectrum of benz[a]anthracene (this work) compared to high–resolution gas–phase IR absorption spectra obtained in a molecular beam (this work).

ID	sym	exp[26]	rel. I[26]	anharm	rel. I	components	I source
a	a′	3087.8	0.37	3078.6	0.38	ν_2	ν_1
						ν_4	ν_2
						$\nu_{13} + \nu_{22}$	ν_3
						$\nu_{14} + \nu_{22}$	
b	a′	3079.0	0.69	3071.7	0.59	ν_1	ν_1
						ν_3	ν_2
						$\nu_{15} + \nu_{21}$	ν_3
c	a′	3063.8	1	3059.0	0.70	ν_2	ν_5
						ν_4	ν_2
						ν_5	
						ν_7	
						$\nu_{15} + \nu_{21}$	
						$\nu_{15} + \nu_{20}$	
						$\nu_{14} + \nu_{22}$	
d	a′	3047.8	0.73	3050.2	1	ν_5	ν_5
						$\nu_{14} + \nu_{24}$	
e	a′	3036.8	0.57	3030.7	0.48	$\nu_{13} + \nu_{24}$	ν_3
						$\nu_{17} + \nu_{20}$	ν_4
							ν_5
							ν_6
f	a′	3017.1	0.20	3012.0	0.14	$\nu_{17} + \nu_{21}$	ν_3
						$\nu_{14} + \nu_{25}$	ν_{12}
						$\nu_{15} + \nu_{24}$	

Table 4.1 Line positions [cm^{-1}], relative intensities, dominant resonant components, and origin of intensities for the bands of the benz[a]anthracene in the high–resolution gas–phase IR absorption spectra obtained in a molecular beam (this work) and the theoretical anharmonic spectrum (this work) as shown in figure 4.12.

Mode	Freq	Symm	Description
ν_1	3194.66	a′	bay symm CH stretch
ν_2	3185.43	a′	non-bay quartet symm CH stretch
ν_3	3183.64	a′	bay symm CH stretch
ν_4	3174.57	a′	bay asymm CH stretch
ν_5	3173.06	a′	non-bay quartet asymm CH stretch/duo CH stretch
ν_6	3172.62	a′	duo CH stretch/non-bay quartet asymm CH stretch/bay asymm CH stretch
ν_7	3166.93	a′	bay quartet CH stretch/bay asymm CH stretch
ν_{12}	3151.39	a′	non-bay singlet/non-bay duo asymm CH stretch
ν_{13}	1659.10	a′	“anthracene” edge CC stretch
ν_{14}	1651.83	a′	outer corner CC stretch
ν_{15}	1640.63	a′	“benzene” edge CC stretch
ν_{17}	1591.75	a′	ring fusing carbons CC stretch
ν_{20}	1508.64	a′	duo/non-bay quartet CH bend
ν_{21}	1482.50	a′	duo/bay quartet CH bend
ν_{22}	1467.65	a′	quartet/quartet CH bend
ν_{24}	1438.95	a′	duo CH bend
ν_{25}	1410.64	a′	singlet CH bend

Table 4.2 Mode descriptions and harmonic frequencies [cm^{-1}] of the IR active modes and modes involved in IR active combination bands/resonances identified in the CH–stretching region of benz[a]anthracene.

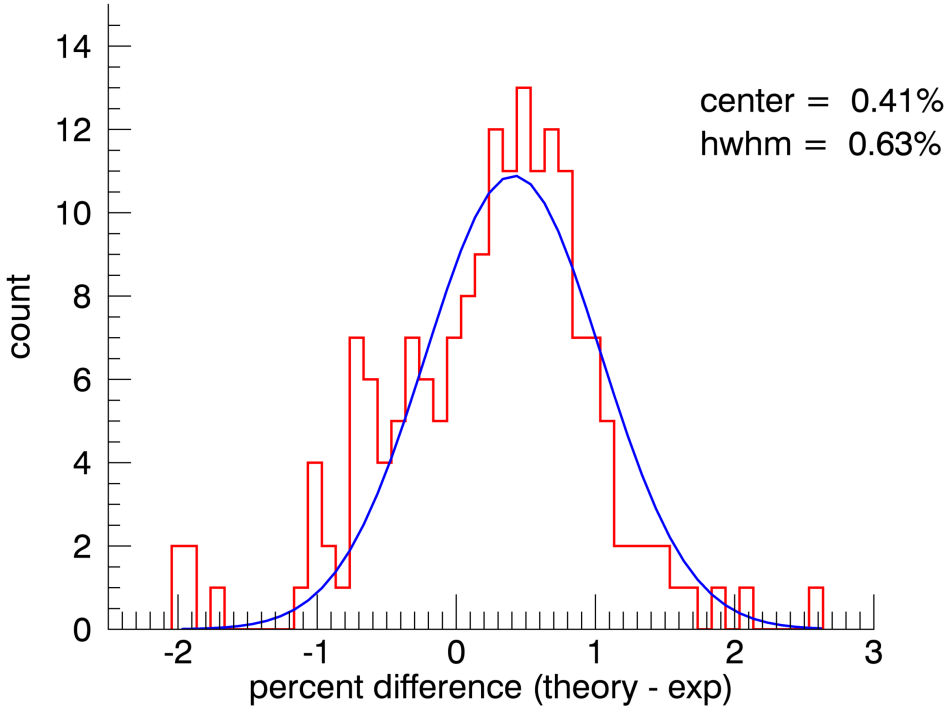

Figure 4.4 Histogram showing the percent differences between the line positions of the anharmonic theory (this work) and (from top to bottom) the MIS experiments for all five PAH species combined.

Molecule	MIS	I	NIST	I	C–H	I
benz[a]anthracene	0.67	66.5	1.02	38.3	0.19	21.7
chrysene	0.72	75.2	0.74	43.2	0.12	40.9
phenanthrene	0.47	53.9	0.55	68.5	0.21	39.7
pyrene	0.73	128	0.97	83.1	0.14	37.8
triphenylene	0.67	44.4	0.85	126	0.15	44.5

Table 4.3 Average absolute percent difference in line positions and relative intensities between the MIS, low–resolution high–temperature gas–phase (NIST), and the high–resolution low–temperature gas–phase (C–H) and the corresponding convolved theoretical anharmonic spectra of this work.

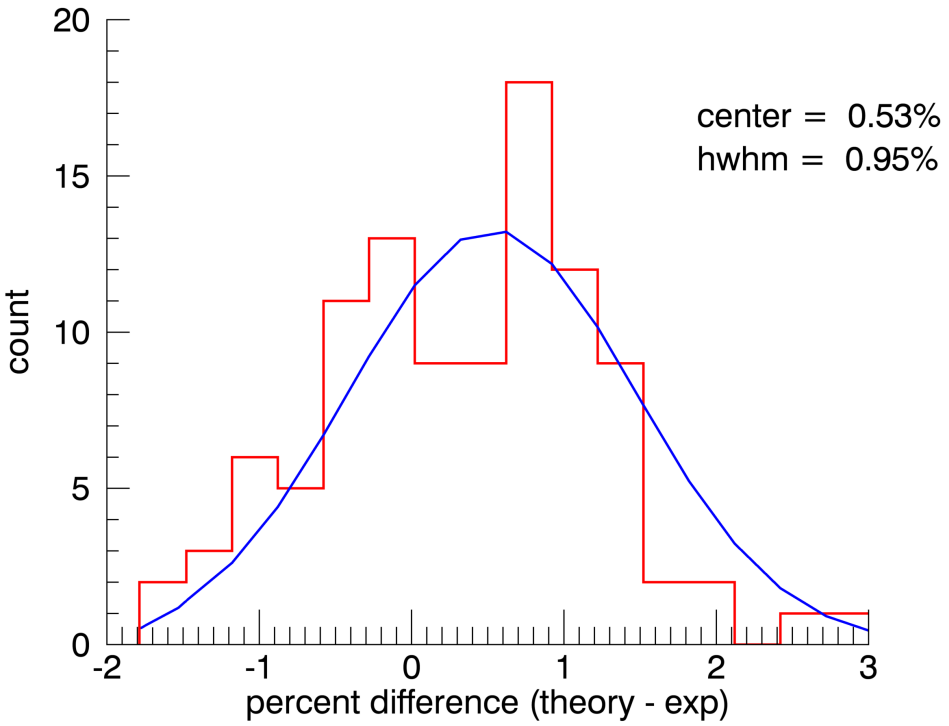

Figure 4.5 Histogram showing the percent differences between the line positions of the anharmonic theory (this work) and (from top to bottom) the NIST gas–phase experiments for all five PAH species combined.

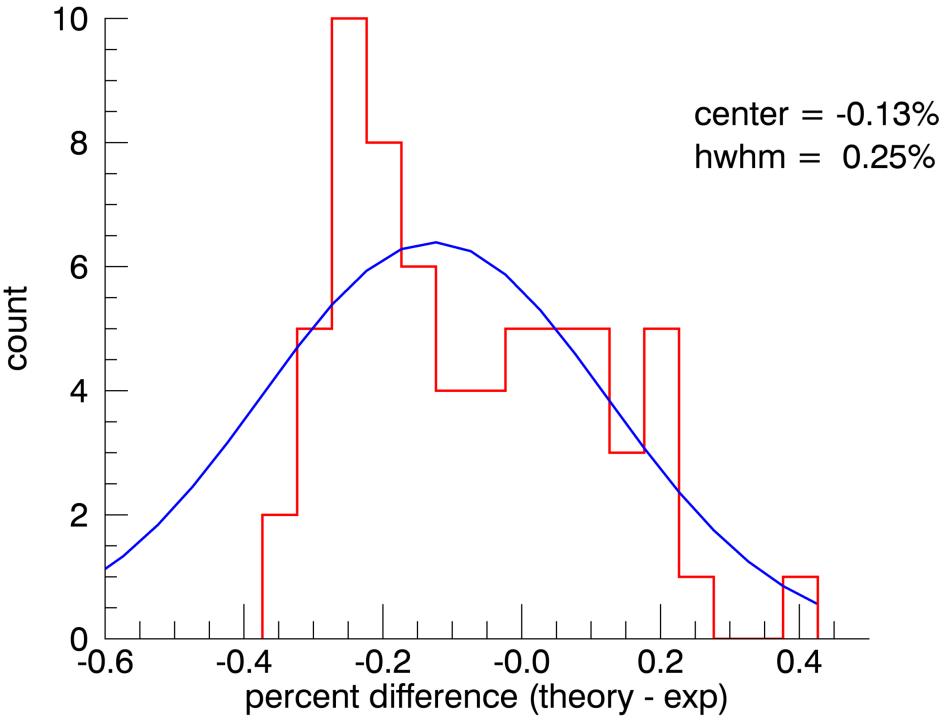

Figure 4.6 Histogram showing the percent differences between the line positions of the anharmonic theory (this work) and (from top to bottom) the low–temperature high–resolution gas–phase experiments for all five PAH species combined.

from the gas phase by 0.21% ±0.87%. The theoretical line positions in this work can therefore be determined accurately to within experimental limitations of MIS spectroscopy.

The average absolute percent differences in relative band intensities (relative to the peak intensity of the strongest out–of–plane C–H mode) between the MIS spectra and the convolved theoretical spectra are given in table 4.3 for each molecule. Matrix interaction effects on band intensities are not as well known as are line positions. However, since the largest deviations are seen for the weakest bands it is plausible that matrix effects are indeed occurring. Nevertheless, overall intensity features match well enough between theory and experiment that line assignment is generally unambiguous.

With the inclusion of anharmonicity the theoretical spectra now can reproduce the large number of combination bands with significant intensities that appear in the experimental spectra. From ~1200 – 1600 cm^{-1} there are a number of combination bands interspersed with the fundamental bands. These include in–plane ring deformations + in–plane ring deformations, out–of–plane C–H bends + out–of–plane drumheads, and out–of–plane C–H bends + out–of-plane C–C bends. The region from ~1600 – 2000 cm^{-1} is dominated by out–of–plane C–H bend + out–of–plane C–H bend combination bands; no fundamentals, and no other types of combination bands have appreciable intensity in this region.

4.5.2 High–temperature gas–phase

Excellent agreement between the low–resolution gas–phase spectra and the convolved anharmonic spectra was also achieved. See the supplemental material for figures of the theoretical spectra compared to experiment, as well as tables listing the band positions, and relative intensities.

The average absolute percent differences in line positions between the high–temperature gas–phase experimental spectra are given in table 4.3 for each molecule. Figure 4.5 shows a histogram of the percent differences between the line positions of the anharmonic theory and the high–temperature gas–phase for all five species combined. This leads to a Gaussian distribution with the average deviation being 0.53% ±0.95%. Using the temperature dependance linear fit equations of ref. 47 (using the pyrene and coronene data in this region) the expected average deviation due to temperature is calculated to be 0.52%. The theoretical line positions in this work can therefore be considered accurate to within temperature dependent shifts.

The average absolute percent differences in relative band intensities (relative to the peak intensity of the strongest out–of–plane C–H mode) between the high–temperature gas–phase experimental spectra and the convolved theoretical spectra is given in table 4.3 for each molecule. Temperature effects and line widths make intensity comparison unreliable. Nevertheless, as in the MIS case overall intensity features match well enough between theory and experiment that spectral feature assignment is unambiguous.

4.5.3 C–H stretching region (low–temperature gas–phase)

A high level of qualitative and quantitative agreement between theory and experiment was achieved for the low–temperature gas–phase experiments. See the supplemental material for figures of the theoretical spectra compared to experiment, as well as tables listing the band positions and assignments, relative intensities, and dominant resonances with mode descriptions.

The average absolute percent difference in line positions between the low–temperature high–resolution gas–phase experimental spectra in the C–H stretching region and the convolved theoretical spectra is given in table 4.3 for each molecule. Figure 5.4 shows a histogram of the percent differences between the line positions of the anharmonic theory and the high–resolution low–temperature gas–phase spectra for all five species combined. The number of bands observed for the five species in the C–H stretching region are limited, as such the statistics on this region are less rigorous. With this in consideration, this leads to a tentative Gaussian distribution with the average deviation being -0.13% ±0.25%. Agreement is best for the low–temperature high–resolution gas–phase data where physical perturbations are minimized.

The average absolute percent differences in relative band intensities (relative to the peak intensity of the strongest band in the C–H stretching region of each molecule) between the low–temperature high–resolution gas–phase experimental spectra and the convolved theoretical spectra is given in table 4.3 for each molecule. Again, agreement is best for the low–temperature high–resolution gas–phase data where physical perturbations are minimized.

This level of agreement in the C–H stretching region provides validation for the theoretical approach used in this work. It is possible that the remaining small deviations in line position and intensities between theory and experiment could be explained by the level of theory used. We therefore performed an MP2 with a cc-pVDZ basis set anharmonic analysis on naphthalene. After performing these calculations a slight improvement in some line positions was seen, but many experimental bands were still unexplained (possible triple combination bands[25]) or not improved at all. This leads to the conclusion that it may be more beneficial to include additional anharmonic terms (quintic, sextic, etc.), than to increase the level of theory. It should be noted that due to the size of PAHs, both raising the level of theory or including additional anharmonic terms is currently computationally not yet feasible.

The anharmonic analysis shows that resonances play a dominant role in describing the C–H stretching region of PAHs. Harmonic calculations predict only a handful of active modes in this region, while the experimental results show many. These additional modes were found to occur due to mainly type two Fermi resonances. It was also found that the strong resonances in this region *always* occur between one C–H stretching fundamental in resonance with an in–plane C–H bending mode in combination with an in–plane C–C stretching mode (see appendix for mode descriptions). Combinations between two in–plane C–H bends or two in–plane C–C stretches do not show strong coupling to the C–H stretching modes, even though the sum of their energies would put them in range to resonate in a

type two Fermi resonance.

4.5.4 Astrophysical implications

This study, in conjunction with our previous work[105] demonstrates the need for anharmonicities to be taken into account when studying astronomical IR PAH spectra. Again, we see how the current modelling of the AIBs can fall short due to the poor reliability of harmonic IR spectra.

The C–H stretching region is especially problematic as the shape and strength of the bands are controlled by resonances. This region can therefore only be understood properly by introducing anharmonicities to models and using an appropriate treatment of resonant states. This conclusion is even more important in the context of the upcoming launch of the James Webb Space Telescope, which will provide high–resolution spectra of this spectral region. Up until now harmonic IR models have sufficed due to the lack of high–resolution astronomical observations of this region, but it is clear that these will not suffice when high-resolution data will become available. This short-coming, in turn, will also be of major impact on the usefulness of astronomical models.

The pure combination band region is controlled by C–H out–of–plane + C–H out–of–plane combination bands. This region can also only be explained by introducing anharmonicities to models. These features have been observed in astronomical observations[101] and since this region is controlled by only C–H out–of–plane modes it may provide an additional means of characterizing the edge structure of astronomical PAHs. Investigations are currently underway.

Temperature effects, emission models, and PAH destruction models are also greatly affected by including anharmonicities. All of these properties are affected by the density of states of excited PAHs. Introducing anharmonicities dramatically changes the complexity of the available states. Investigations on these effects on the theoretical spectra are currently underway.

4.6 Conclusions

Five non–linear PAHs were considered in this work: benz[a]anthracene, chrysene, phenanthrene, pyrene, and triphenylene. All theoretical spectra show excellent agreement in band positions with the three types of experiments shown. The theoretical band positions have been shown to be in agreement with the MIS data to within an average of 0.41% with a standard deviation of 0.63%, with high–temperature gas–phase to within an average of 0.53% with a standard deviation of 0.95%, and with low–temperature gas–phase in the C–H stretching region to within an average of -0.13% with a standard deviation of 0.25%. The good comparison with the high–resolution, low–temperature gas–phase spectra is particularly gratifying as these spectra provide “ground truth”. Further, this is the region that is theoretically the most challenging due to the dominance of Fermi resonances, and hence we take it that this good comparison implies that in the absence of gas–phase data anharmonic calculations are the instrument of choice when analyzing astronomical observations.

Intensity comparison between the anharmonic IR spectra and experiments shows moderate agreement for the MIS and high-temperature gas-phase data. Temperature effects and matrix interaction effects could be responsible for the larger discrepancies in intensities. High–resolution data where these effects are absent show better agreement. This underlines the need for experimental low–temperature gas–phase spectra in the complete IR range. Triphenylene (see section 4.7) shows intensity problems, both due to a poorly estimated QFF and erroneously calculated anharmonic intensities.

The reduction of symmetry to handle a symmetric top molecule, such as triphenylene, with the anharmonic approach presented in this work has been shown to have limitations, but the results are surprisingly good in the C–H stretching region. Further investigation into other highly symmetric molecules as well as other techniques for dealing with symmetric tops are warranted. SPECTRO is able to handle symmetric top molecules, but there is a potential issue for non–degenerate, non–totally symmetric modes which must be handled carefully[112]. Symmetric top molecules are of special importance since many current astronomical models, both theoretical and experimental, use coronene ($\mathcal{D}_{6h}$ symmetry) as a typical PAH stand–in. Efforts are currently underway to apply the methods described in this work to coronene in order to better understand the issues that arise.

Compared to harmonic calculations (see ref. 26 for a comparison in the C–H stretching region) the anharmonic calculations provide a vast improvement. Harmonic frequencies are off by typically over 4%, whereas the anharmonic frequencies are off by less than 1%. This level of agreement eliminates the need for an empirical scaling factor to bring harmonic calculations in line with experiment. Harmonic calculations can also not explain the large number of bands seen in the C–H stretching region (type two Fermi resonances), or reproduce any of the large number of bands seen in the 1600–2000 cm^{-1} region (combination bands), while anharmonic calculations can. These conclusions are important as they imply that also for compounds for which it so far has not been possible to record experimental IR spectra it is possible to use theoretically predicted spectra as a reliable proxy. This, in turn, paves the way for a full in–silico screening of PAH models.

Patterns are beginning to arise with the anharmonic effects on the spectra of PAHs, especially in the resonance structure of the C–H stretching region and pure combination band region. *All* strong bands occurring in the C–H stretching region involve type two Fermi resonances ($\nu_a + \nu_b \approx \nu_c$) consisting of C–C stretching modes in combination with in–plane C–H bending modes resonating with in–plane C–H stretching fundamentals. Likewise, *all* strong bands occurring in the pure combination band region are combinations of two out–of–plane C–H bends. This, along with symmetry considerations, greatly simplifies the number of interacting modes to consider, and accounts for most of the anharmonic effects observed. This holds promise for generalizing anharmonic effects in order to avoid full anharmonic QFF analysis for many individual PAH species. However, a larger set of test cases, including larger PAHs sizes and various molecular symmetries, is necessary in order to further develop these generalizations and techniques. Efforts are currently underway. PAH derivatives (methylated, hydrogenated, dehydrogenated, nitrogen–substituted, cations, anions, etc.) are also of great interest to

astronomers. For that reason this work is also being extended into investigating anharmonic effects on these species.

Acknowledgments

The authors would like to thank the two anonymous reviewers for their helpful comments that improved the clarity of the manuscript. The spectroscopic study of interstellar PAHs at Leiden Observatory have been supported through the Advanced European Research Council Grant 246976, a Spinoza award, and through the Dutch Astrochemistry Network funded by the Netherlands Organization for Scientific Research, NWO. Computing time has been made available by NWO Exacte Wetenschappen (project MP–270–13 and MP–264) and calculations were performed at the LISA Linux cluster of the SurfSARA supercomputer center in Almere, The Netherlands. AC acknowledges NWO for a VENI grant (639.041.543). AP acknowledges NWO for a VIDI grant (723.014.007). XH and TJL gratefully acknowledge support from the NASA 12–APRA12–0107 grant. XH acknowledges the support from NASA/SETI Co–op Agreement NNX15AF45A. This material is based upon work supported by the National Aeronautics and Space Administration through the NASA Astrobiology Institute under Cooperative Agreement Notice NNH13ZDA017C issued through the Science Mission Directorate.

4.7 Appendix

Triphenylene

Triphenylene is a symmetric top, with $\mathcal{D}_{3h}$ symmetry. Gaussian09 cannot handle symmetric tops at the anharmonic level. Therefore, to circumvent this triphenylene was approximated as an asymmetric top by slightly perturbing the masses of two opposing carbon atoms of the central ring from 12 au to 12.01 au, consequently lowering the symmetry to C_{2v}.

By perturbing the masses slightly the symmetry of a molecule breaks, while preserving the symmetry of the potential energy surface as much as possible. Perturbing the masses resulted in the degenerate harmonic modes splitting by ~0.01%, leaving the potential with nearly the same symmetry at the harmonic level. The symmetry of the potential at the anharmonic level can be estimated by comparing the cubic force constants [113]. For degenerate modes of a symmetric top, the normal coordinate cubic force constants are related by

$$F_{aaa} = -F_{abb} \tag{4.1}$$

where a and b are components of a degenerate normal mode, and a is symmetric with respect to the operations of the point group while b is antisymmetric with respect to one operation.

For triphenylene the comparisons between the non–zero cubic force constants of the degenerate modes (14 pairs) shows a percent difference of 28% on average.

The sign of the cubic force constants are all found to be correct between pairs. This result shows that the symmetry of the QFF of triphenylene is more broken than ideal, most likely due to the level of theory used.

Performing the VPT2 anharmonic analysis with SPECTRO with this slightly broken symmetry QFF, it was found that there is moderate agreement in the 1600 – 2000 cm^{-1} region. Major deviations however, can be seen in between 1400 and 1550 cm^{-1} (see the supplemental material). The appearance of additional strong bands in this region (and a few minor bands in the 1600 – 2000 cm^{-1} region) are a result of the over–estimation of resonance strengths between modes caused by the breakdown of the QFF. For bands <1400 cm^{-1} major deviations are found with the anharmonic intensities reported by Gaussian09. Some anharmonic bands were found to have intensities two, or even sometimes three, orders of magnitude too high (not shown). For the <1400 cm^{-1} region we therefore reverted to using the harmonic intensities in our analysis. The extremely large intensities are likely due to "resonances" between modes that are actually different components of a degenerate vibration and are a byproduct of using an asymmetric top formulation for a symmetric top molecule.

The C–H stretching region, on the other hand, shows excellent agreement with experiment. This agreement is due to the fact that the parts of the QFF affecting resonances between C–H in–plane modes appear to largely unaffected by the symmetry lowering. Harmonic intensities are being utilized in this region for all molecules, so spurious anharmonic intensities are already excluded. The lowering of the symmetry of the molecule also led to changes in the symmetries of the individual bands, complicating assigning symmetries to individual bands, especially combination bands. Therefore, no symmetries are listed in the supplemental material.

4.8 Supplemental Material

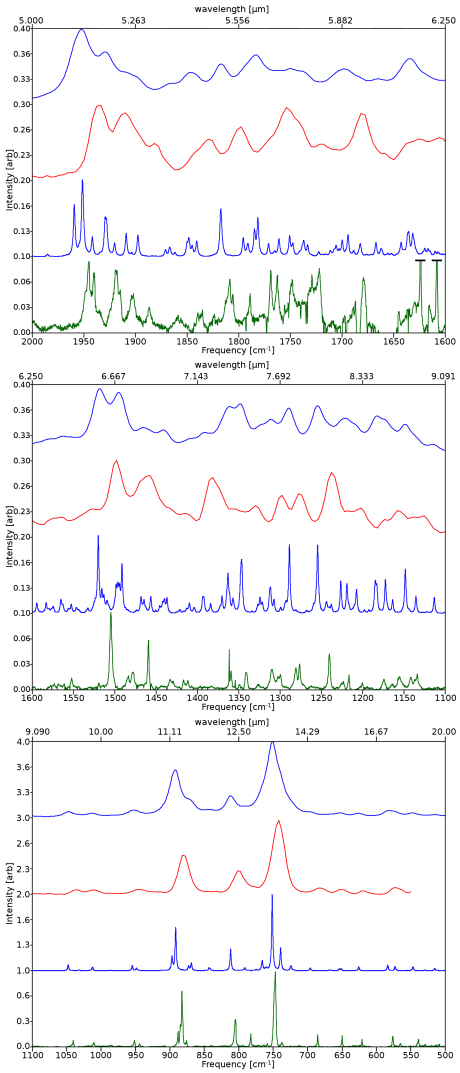

Figure 4.7 Comparison of the IR spectrum of benz[a]anthracene between the matrix–isolation experimental at 15 K (green, bottom spectrum of each panel), the theoretical anharmonic (this work) convolved with a FWHM of 2 cm^{-1} (blue, bottom middle spectrum of each panel), the gas–phase experimental at 300 K[21] (red, top middle spectrum of each panel), and the theoretical anharmonic (this work) convolved with a FWHM of 18 cm^{-1} (blue, top spectrum of each panel). Three spectral ranges are shown. Each range has its intensities normalized to the local maximum to enhance details. Water contaminant line intensities have been truncated.

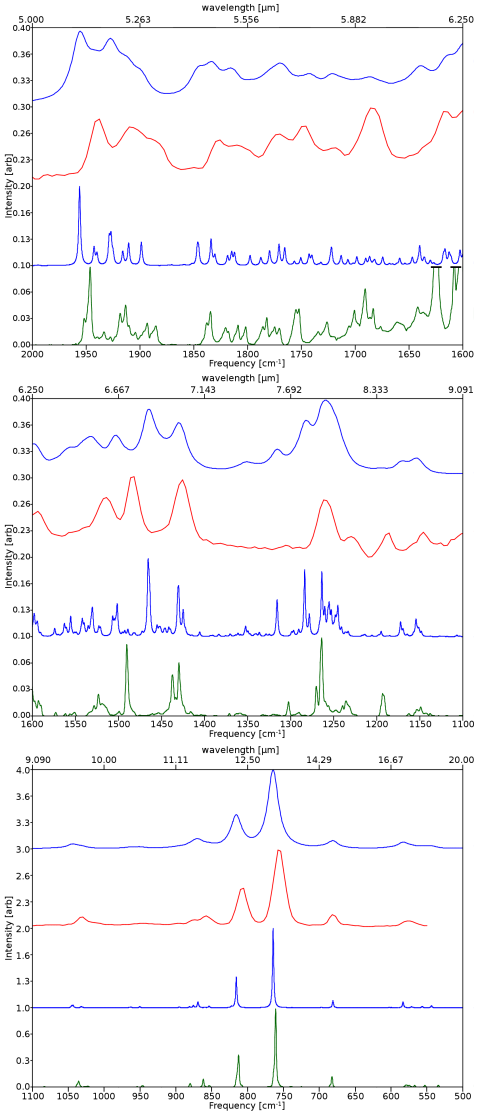

Figure 4.8 Comparison of the IR spectrum of chrysene between the matrix–isolation experimental at 15 K (green, bottom spectrum of each panel), the theoretical anharmonic (this work) convolved with a FWHM of 2 cm^{-1} (blue, bottom middle spectrum of each panel), the gas–phase experimental at 300 K[21] (red, top middle spectrum of each panel), and the theoretical anharmonic (this work) convolved with a FWHM of 18 cm^{-1} (blue, top spectrum of each panel). Three spectral ranges are shown. Each range has its intensities normalized to the local maximum to enhance details; see table 4.4 for true relative intensities. Water contaminant line intensities have been truncated.

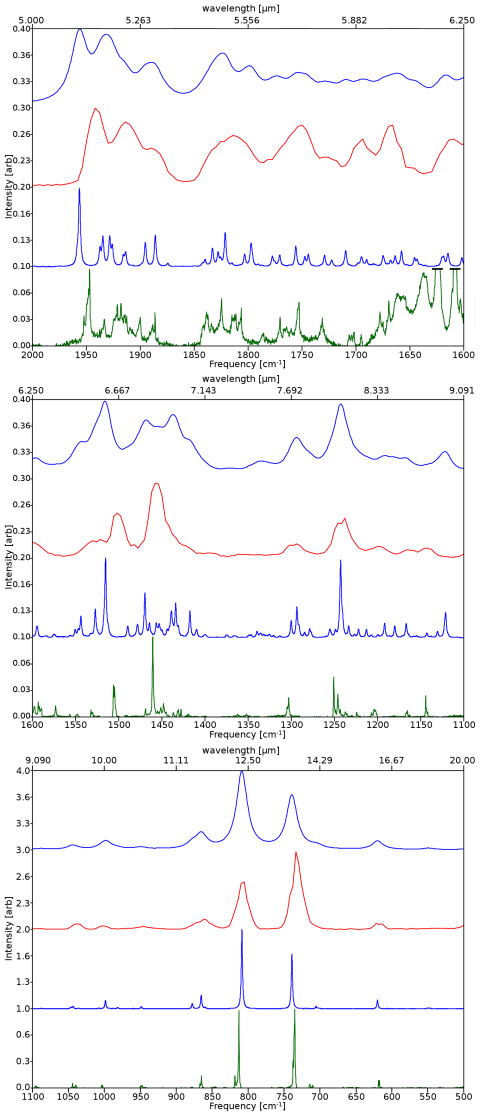

Figure 4.9 Comparison of the IR spectrum of phenanthrene between the matrix–isolation experimental at 15 K (green, bottom spectrum of each panel), the theoretical anharmonic (this work) convolved with a FWHM of 2 cm^{-1} (blue, bottom middle spectrum of each panel), the gas–phase experimental at 300 K[21] (red, top middle spectrum of each panel), and the theoretical anharmonic (this work) convolved with a FWHM of 18 cm^{-1} (blue, top spectrum of each panel). Three spectral ranges are shown. Each range has its intensities normalized to the local maximum to enhance details; see table 4.4 for true relative intensities. Water contaminant line intensities have been truncated.

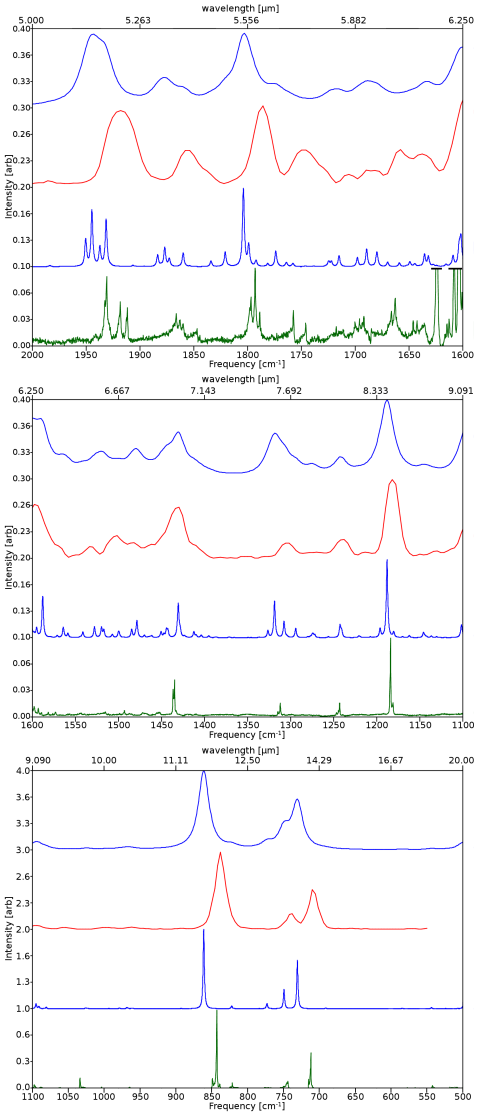

Figure 4.10 Comparison of the IR spectrum of pyrene between the matrix–isolation experimental at 15 K (green, bottom spectrum of each panel), the theoretical anharmonic (this work) convolved with a FWHM of 2 cm^{-1} (blue, bottom middle spectrum of each panel), the gas–phase experimental at 300 K[21] (red, top middle spectrum of each panel), and the theoretical anharmonic (this work) convolved with a FWHM of 18 cm^{-1} (blue, top spectrum of each panel). Three spectral ranges are shown. Each range has its intensities normalized to the local maximum to enhance details; see table 4.4 for true relative intensities. Water contaminant line intensities have been truncated.

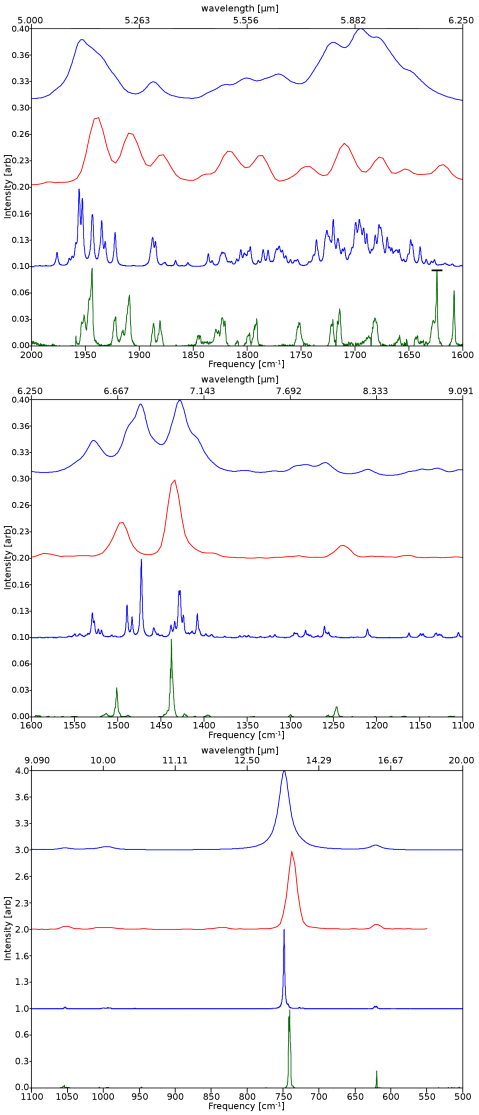

Figure 4.11 Comparison of the IR spectrum of triphenylene between the matrix–isolation experimental at 15 K (green, bottom spectrum of each panel), the theoretical anharmonic (this work) convolved with a FWHM of 2 cm^{-1} (blue, bottom middle spectrum of each panel), the gas–phase experimental at 300 K[21] (red, top middle spectrum of each panel), and the theoretical anharmonic (this work) convolved with a FWHM of 18 cm^{-1} (blue, top spectrum of each panel). Three spectral ranges are shown. Each range has its intensities normalized to the local maximum to enhance details; see table 4.4 for true relative intensities. Water contaminant line intensities have been truncated.

Table 4.4: MIS line positions [cm^{-1}] and relative intensities [arb], and corresponding theoretical line positions and relative intensities determined from the simulated spectrum (convolved with a FWHM of 2 cm^{-1} Fig. 4.7 – 4.10). Bands are arranged by vibrational mode description, determined from theoretical data. Similar spectral features between species are aligned across the rows.

Benz[a]anthracene				Chrysene				Phenanthrene				Pyrene				Triphenylene			
Matrix	I	Theory	I	Matrix	I	Theory	I	Matrix	I	Theory	I	Matrix	I	Theory	I	Matrix	I	Theory	I
ring stretch/deformations																			
				534.4	0.02	543.9	0.03												
576.6	0.14	583.9	0.08	567.4	0.02	571.7	0.01												
621.3	0.10	626.0	0.05	574.8	0.02	-	-	618.2	0.08	620.3	0.11					620.0	0.27	621.5	0.06
650.2	0.15	651.4	0.03																
				682.7	0.13	681.3	0.09												
								710.6	0.03	705.7	0.03								
758.8	0.04	759.9	0.05																
				853.7	0.02	854.1	0.02												
				880.4	0.05	875.9	0.03												
																993.4	0.01	994.2	0.01
								1003.3	0.04	998.7	0.10					1005.8	0.01	999.8	0.01
out–of–plane C–H bends																			
539.5	0.09	547.2	0.05																
565.6	0.04	573.1	0.05	553.2	0.02	556.8	0.02												
685.6	0.15	696.4	0.04																
737.7	0.05	739.5	0.30																
747.8	1	751.7	1	761.2	1	764.7	1	735.7	1	739.4	0.69	730.9	0.61	741.0	1	748.9	1		
782.8	0.15	791.5	0.04									744.1	0.09	749.6	0.24				
805.4	0.36	812.1	0.29	813.3	0.41	816.0	0.39	813.1	0.88	808.9	1	843.0	1	861.4	1				
882.7	0.79	891.9	0.57	862.1	0.09	869.5	0.08	865.4	0.12	865.6	0.17								
944.3	0.03	948.9	0.03	946.8	0.02	950.6	0.02	948.5	0.03	948.8	0.02	964.8	0.01	968.6	0.02	947.4	0.02	956.6	0.01
952.1	0.07	954.9	0.06	954.8	0.01	962.9	0.01												
out–of–plane C–C bends																			
				578.9	0.03	583.6	0.07												
												712.3	0.36						
in–plane C–C bends																			
												821.7	0.07	822.4	0.04				
in–plane C–H bends																			
1011.0	0.05	1012.7	0.05																
								1040.0	0.04	1036.6	0.01								
1040.8	0.08	1048.0	0.08									1033.9	0.12	-	-	1054.5	0.03	1053.5	0.02
												1088.4	0.01	1081.0	0.02				

Table 4.4 – continued from previous page

Benz[a]anthracene				Chrysene				Phenanthrene				Pyrene				Triphenylene			
Matrix	I	Theory	I	Matrix	I	Theory	I	Matrix	I	Theory	I	Matrix	I	Theory	I	Matrix	I	Theory	I
1134.9	0.03	1113.7	0.02																
1142.1	0.03	1135.7	0.03	1149.0	0.01	1154.7	0.02	1144.2	0.04	1121.4	0.02								
1155.5	0.03	1148.7	0.07	1153.4	0.01	1172.5	0.02												
1164.6	0.01	1172.7	0.05					1166.2	0.01	1167.0	0.02								
1174.6	0.02	1184.9	0.05																
1200.7	0.01	1207.6	0.04									1184.3	0.18	1188.3	0.14				
1276.5	0.06	1288.9	0.10					1250.9	0.11	1243.0	0.09					1246.7	0.04	1260.6	0.01
1310.0	0.05	1311.9	0.04																
1413.9	0.01	1409.9	0.02																
1459.6	0.13	1456.8	0.03																
in–plane C–C stretch																			
				1023.1	0.01	1032.2	0.02												
				1036.0	0.08	1043.5	0.05	1044.6	0.07	1046.8	0.02								
				1264.3	0.12	1283.9	0.06					1243.4	0.03	1242.9	0.02				
				1302.8	0.02	1315.8	0.04	1303.6	0.04	1293.7	0.03	1312.4	0.03	1319.0	0.06	1299.9	0.01	1294.2	0.01
1341.2	0.05	1346.7	0.08																
1360.7	0.04	1363.2	0.06																
				1416.2	0.01	1425.1	0.03	1431.5	0.02	1439.2	0.03					1422.9	0.01	1407.9	0.02
				1430.0	0.08	1430.4	0.05					1435.1	0.10	1430.7	0.06	1438.0	0.25	1428.5	0.04
				1437.7	0.06	1465.8	0.08												
1478.5	0.04	1491.5	0.06					1469.2	0.02	1478.3	0.02								
				1490.7	0.11	1501.4	0.03	1506.3	0.09	1515.5	0.09	1493.5	0.01	1478.8	0.03	1501.3	0.09	1472.9	0.06
1519.5	0.02	1516.0	0.04	1523.5	0.03	1539.9	0.01	1531.4	0.01	1544.1	0.02					1514.2	0.01	1489.4	0.03
				1551.3	0.01	1542.2	0.02												
				1590.1	0.01	1594.5	0.02					1604.4	0.08	1588.2	0.07				
ring stretch/deform + ring stretch/deform (combination bands)																			
												1097.3	0.03	1095.1	0.06				
1240.5	0.09	1254.7	0.10	1235.9	0.02	1245.4	0.03	1224.2	0.01	1213.2	0.01								
1326.4	0.01	1321.9	0.01																
								1427.9	0.02	1434.2	0.04					1396.2	0.01	1391.4	0.01
ring breathing																			
				1192.8	0.03	1195.1	0.01	1203.5	0.02	1192.0	0.02								
out–of–plane bend + drum head (combination bands)																			
1217.0	0.03	1226.7	0.05																
1224.7	0.02	1238.2	0.01																
				1240.4	0.01	1255.5	0.04												
				1246.8	0.01	1264.0	0.07												
1301.5	0.03	1307.6	0.02																
1505.0	0.20	1520.3	0.12																
out–of–plane C–H bend + out–of–plane C–C bend (combination bands)																			
1281.2	0.05	1299.6	0.10	1270.4	0.04	1278.5	0.02												

Table 4.4 – continued from previous page

Benz[a]anthracene				Chrysene				Phenanthrene				Pyrene				Triphenylene			
Matrix	I	Theory	I	Matrix	I	Theory	I	Matrix	I	Theory	I	Matrix	I	Theory	I	Matrix	I	Theory	I
								1436.7	0.01	1444.1	0.01								
1432.0	0.02	1437.1	0.02					1448.4	0.04	1453.4	0.02								
								1451.5	0.03	1456.7	0.02								
1484.4	0.03	1496.5	0.04									1452.3	0.01	1444.3	0.02	1488.2	0.01	1458.2	0.01
1552.5	0.02	1565.6	0.02																
out–of–plane C–H bend + out–of–plane C–H bend (combination bands)																			
																1627.2	0.01	1639.7	0.01
				1641.9	0.02	1640.3	0.02	1637.2	0.04	-	-								
								1660.6	0.02	-	-								
								1669.7	0.01	1663.8	0.01	1663.0	0.02	-	-				
1679.2	0.03	1667.4	0.02	1690.8	0.02	1686.9	0.01	1678.0	0.01	1675.0	0.01					1681.8	0.01	1676.9	0.02
				1701.0	0.01	1698.7	0.01												
1722.2	0.03	1733.5	0.01					1731.4	0.01	1729.4	0.01					1714.4	0.01	1720.3	0.02
1728.9	0.03	1737.3	0.02																
1747.4	0.02	1750.9	0.02																
				1755.5	0.01	1743.1	0.01	1753.8	0.01	1756.0	0.02					1752.1	0.01	1772.1	0.01
1763.1	0.03	1781.6	0.04									1757.5	0.01	1774.0	0.02				
1769.1	0.03	1785.1	0.03																
1789.1	0.02	1795.7	0.02	1782.5	0.01	1765.7	0.02					1793.2	0.03	1804.1	0.11	1792.2	0.01	1797.4	0.01
												1797.1	0.02	1799.2	0.03				
				1802.5	0.01	1787.7	0.01												
1809.5	0.02	1817.6	0.05	1809.6	0.01	1797.9	0.01	1812.7	0.01	1803.5	0.01								
				1820.7	0.01	1834.2	0.01	1825.4	0.01	1821.5	0.03					1823.2	0.01	1822.4	0.01
				1834.8	0.01	1846.3	0.02	1837.7	0.01	1833.2	0.02								
1837.9	0.01	1841.0	0.02																
1858.8	0.01	1867.2	0.01									1866.5	0.01	1860.0	0.02				
																1880.9	0.01	1885.1	0.01
1887.1	0.01	1897.8	0.02	1886.1	0.01	1898.9	0.02									1887.0	0.01	1888.0	0.01
1903.1	0.02	1909.2	0.02	1893.6	0.01	1910.8	0.02	1900.9	0.01	1895.5	0.02								
								1918.4	0.02	1928.6	0.03	1912.3	0.01	1931.7	0.07	1909.3	0.01	1922.6	0.01
1918.9	0.03	1929.5	0.04	1918.5	0.01	1927.6	0.03					1918.9	0.01	1937.4	0.03	1922.8	0.01	1935.1	0.02
1935.2	0.01	1942.0	0.02									1931.6	0.02	1944.9	0.08				
1940.1	0.04	1951.5	0.09																
1944.2	0.03	1959.5	0.06	1946.4	0.03	1956.3	0.06	1948.5	0.02	1956.6	0.07					1944.1	0.02	1952.9	0.02
																1951.4	0.01	1956.0	0.03
unidentified																			
												1003.8	0.01	-	-				
				1083.6	0.01	-	-												
								1095.4	0.03	-	-								
								1246.2	0.05	-	-								
																1256.4	0.01	-	-

Table 4.4 – continued from previous page

Benz[a]anthracene				Chrysene				Phenanthrene				Pyrene				Triphenylene			
Matrix	I	Theory	I	Matrix	I	Theory	I	Matrix	I	Theory	I	Matrix	I	Theory	I	Matrix	I	Theory	I
								1460.7	0.23	-	-								
								1573.4	0.03	-	-								
				1601.8	0.03	-	-												
water contamination																			
1608.3	0.07	-	-	1608.4	-	-	-	1608.3	0.19	-	-	1608.3	0.05	-	-	1608.4	0.01	-	-
1624.2	0.09	-	-	1624.1	-	-	-	1624.2	0.25	-	-	1624.2	0.11	-	-	1624.2	0.02	-	-

Benz[a]anthracene				Chrysene				Phenanthrene				Pyrene				Triphenylene			
Gas	I	Theory	I	Gas	I	Theory	I	Gas	I	Theory	I	Gas	I	Theory	I	Gas	I	Theory	I
570.9	0.09	582.5	0.10	574.2	0.08	583.6	0.09									620.1	0.07	621.5	0.06
619.2	0.05	624.6	0.05																
649.3	0.06	654.1	0.07					622.0	0.09	620.3	0.11								
685.3	0.07	699.2	0.08	682.0	0.18	681.3	0.11												
742.8	1	751.7	1	758.0	1	764.7	1	732.2	1	739.4	0.70	708.6	0.53	730.9	0.41	737.4	1	748.7	1
798.3	0.28	812.1	0.29									739.5	0.21	749.6	0.26				
879.9	0.54	892.8	0.62	806.0	0.51	816.1	0.43	808.0	0.66	808.9	1	838.1	1	861.3	1				
				858.0	0.16	870.6	0.13	862.8	0.13	865.6	0.23					835.6	0.02	-	-
940.0	0.06	952.4	0.10					945.7	0.03	949.2	0.04	964.8	0.01	967.0	0.04	944.6	0.01	956.4	0.01
1011.4	0.06	1013.4	0.06					1001.2	0.04	998.7	0.12	998.7	0.03	-	-	988.9	0.02	996.3	0.04
1036.9	0.06	1048.0	0.07	1030.0	0.14	1043.5	0.06	1038.3	0.08	1044.0	0.06	1054.2	0.03	-	-	1051.8	0.04	1053.1	0.02
								1090.7	0.01	1086.5	0.02	1095.3	0.05	1094.7	0.10				
1158.5	0.02	1148.7	0.09	1187.9	0.04	1195.9	0.02												
								1143.2	0.01	1133.2	0.03								
								1163.5	0.01	-	-								
1206.3	0.06	1225.5	0.07	1228.0	0.03	-	-	1200.9	0.02	1192.0	0.04								
1237.9	0.13	1255.1	0.12	1259.6	0.09	1258.7	0.16	1241.1	0.07	1243.0	0.12	1182.0	0.13	1188.3	0.14				
1275.9	0.09	1289.7	0.13									1241.3	0.02	1242.9	0.04	1239.0	0.03	1258.3	0.01
								1296.0	0.02	1293.7	0.06	1302.9	0.02	1318.7	0.08				
1327.5	0.05	1322.0	0.06																
1382.5	0.10	1364.2	0.11																
1417.4	0.05	1412.5	0.05																
1462.4	0.12	1463.9	0.06	1426.0	0.12	1430.2	0.11	1457.2	0.16	1469.1	0.10	1432.9	0.08	1430.7	0.08	1434.9	0.18	1425.9	0.08
												1483.0	0.02	-	-				
1498.5	0.12	1494.5	0.16	1482.0	0.11	1464.9	0.06	1500.7	0.09	1516.4	0.12	1504.0	0.04	1479.5	0.04	1496.5	0.08	1476.6	0.08
				1518.0	0.08	1503.4	0.09	1527.8	0.03	1545.6	0.06	1533.8	0.02	1520.0	0.05				
1571.8	0.04	1564.1	0.04																
1630.0	0.03	1621.5	0.05	1594.0	0.07	1599.2	0.07	1607.2	0.03	1617.1	0.03	1595.6	0.08	1595.8	0.11				
												1637.1	0.03	1634.6	0.04	1619.8	0.01	-	-
												1658.5	0.03	-	-				
1681.4	0.05	1697.0	0.06	1684.5	0.06	1686.9	0.03	1667.8	0.04	1659.5	0.04	1685.2	0.02	1688.7	0.04	1687.0	0.01	1687.2	0.09
								1696.5	0.03	1710.3	0.02	1707.2	0.01	1722.1	0.03	1709.5	0.02	-	-
1750.4	0.05	1784.9	0.07	1748.4	0.04	1741.0	0.02	1753.5	0.04	1748.7	0.04	1745.7	0.04	1774.1	0.04	1745.2	0.01	1723.9	0.04
1799.3	0.04	1817.8	0.06	1770.8	0.04	1769.9	0.05					1786.9	0.08	1803.2	0.14	1787.7	0.01	1772.3	0.02
1831.0	0.03	1843.2	0.04	1829.1	0.01	1845.5	0.03	1815.1	0.04	1823.7	0.06	1854.0	0.03	1877.2	0.05	1816.6	0.01	1805.4	0.02
1884.3	0.03	1907.6	0.05					1885.5	0.02	1887.6	0.05					1878.8	0.01	1886.2	0.02
1910.5	0.05	1928.5	0.06	1910.0	0.04	1927.8	0.07	1913.4	0.05	1932.0	0.08					1907.7	0.02	1936.1	0.04
1936.3	0.06	1952.1	0.12	1942.0	0.05	1956.8	0.07	1942.0	0.05	1957.1	0.05	1917.7	0.08	1943.1	0.13	1939.8	0.03	1954.8	0.06

Table 4.5 Gas phase[21] (300K) line positions [cm^{-1}] and relative intensities [arb], and corresponding theoretical line positions and intensities determined from the simulated spectrum (convolved with a FWHM of 18 cm^{-1}, Fig. 4.7 – 4.10). Similar spectral features between species are aligned across the rows.

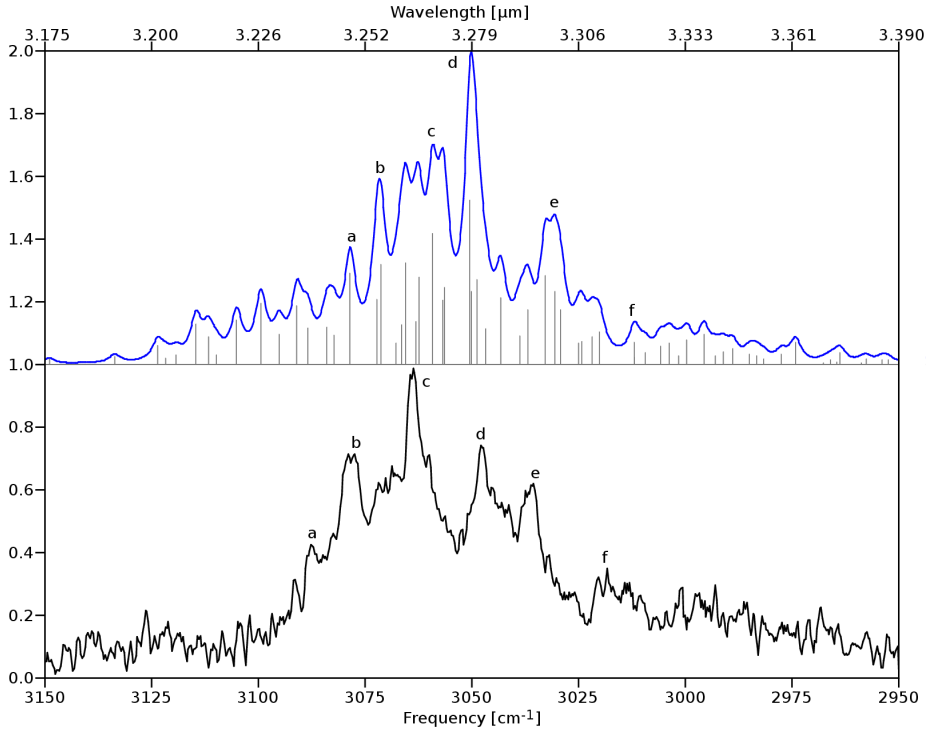

Figure 4.12 Anharmonic QFF IR spectrum of benz[a]anthracene (this work) compared to high–resolution gas–phase IR absorption spectra obtained in a molecular beam (this work).

Mode	Freq	Symm	Description
ν_1	3194.66	a′	bay symm CH stretch
ν_2	3185.43	a′	non-bay quartet symm CH stretch
ν_3	3183.64	a′	bay symm CH stretch
ν_4	3174.57	a′	bay asymm CH stretch
ν_5	3173.06	a′	non-bay quartet asymm CH stretch/duo CH stretch
ν_6	3172.62	a′	duo CH stretch/non-bay quartet asymm CH stretch/bay asymm CH stretch
ν_7	3166.93	a′	bay quartet CH stretch/bay asymm CH stretch
ν_{12}	3151.39	a′	non-bay singlet/non-bay duo asymm CH stretch
ν_{13}	1659.10	a′	“anthracene” edge CC stretch
ν_{14}	1651.83	a′	outer corner CC stretch
ν_{15}	1640.63	a′	“benzene” edge CC stretch
ν_{17}	1591.75	a′	ring fusing carbons CC stretch
ν_{20}	1508.64	a′	duo/non-bay quartet CH bend
ν_{21}	1482.50	a′	duo/bay quartet CH bend
ν_{22}	1467.65	a′	quartet/quartet CH bend
ν_{24}	1438.95	a′	duo CH bend
ν_{25}	1410.64	a′	singlet CH bend

Table 4.6 Mode descriptions and harmonic frequencies [cm^{-1}] of the IR active modes and modes involved in IR active combination bands/resonances identified in the CH–stretching region of benz[a]anthracene.

ID	sym	exp[26]	rel. I[26]	anharm	rel. I	components	I sources
a	a′	3087.8	0.37	3078.6	0.38	ν_2	ν_1
						ν_4	ν_2
						$\nu_{13} + \nu_{22}$	ν_3
						$\nu_{14} + \nu_{22}$	
b	a′	3079.0	0.69	3071.7	0.59	ν_1	ν_1
						ν_3	ν_2
						$\nu_{15} + \nu_{21}$	ν_3
c	a′	3063.8	1	3059.0	0.70	ν_2	ν_5
						ν_4	ν_2
						ν_5	
						ν_7	
						$\nu_{15} + \nu_{21}$	
						$\nu_{15} + \nu_{20}$	
						$\nu_{14} + \nu_{22}$	
d	a′	3047.8	0.73	3050.2	1	ν_5	ν_5
						$\nu_{14} + \nu_{24}$	
e	a′	3036.8	0.57	3030.7	0.48	$\nu_{13} + \nu_{24}$	ν_3
						$\nu_{17} + \nu_{20}$	ν_4
							ν_5
							ν_6
f	a′	3017.1	0.20	3012.0	0.14	$\nu_{17} + \nu_{21}$	ν_3
						$\nu_{14} + \nu_{25}$	ν_{12}
						$\nu_{15} + \nu_{24}$	

Table 4.7 Line positions [cm^{-1}], relative intensities, dominant resonant components, and origin of intensities for the bands of the benz[a]anthracene in the high–resolution gas–phase IR absorption spectra obtained in a molecular beam (this work) and the theoretical anharmonic spectrum (this work) as shown in figure 4.12.

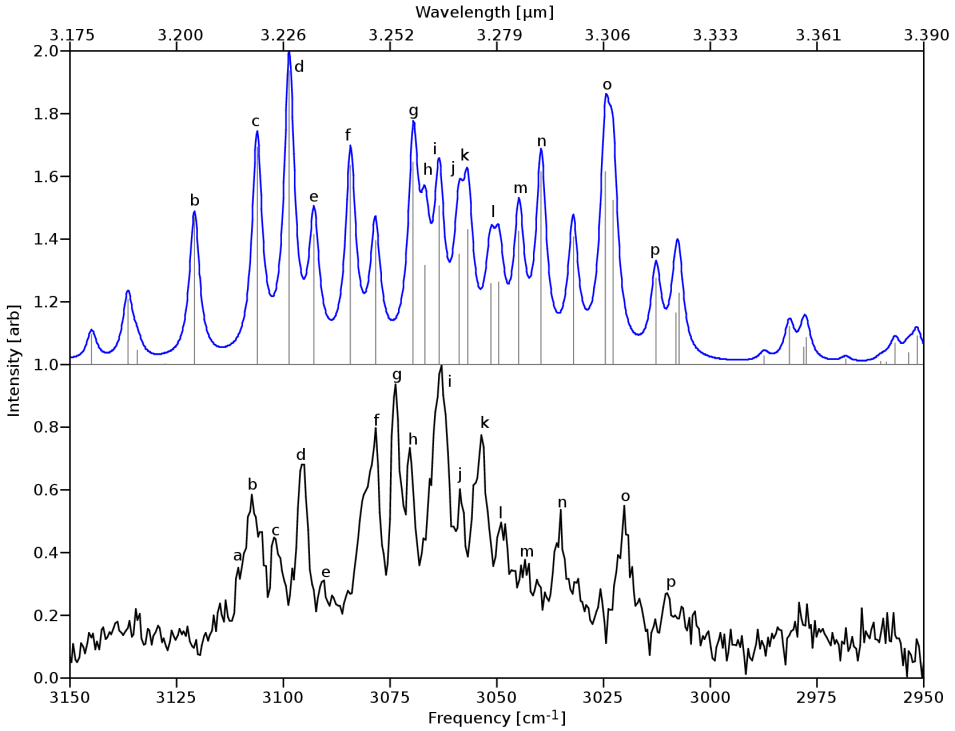

Figure 4.13 Anharmonic QFF IR spectrum of chrysene (this work) compared to high–resolution gas–phase IR absorption spectra obtained in a molecular beam (this work).

Mode	Freq	Symm	Description
ν_2	3207.21	b_u	bays symm CH stretch
ν_3	3191.81	b_u	bays asymm CH stretch
ν_6	3182.58	b_u	quartets asymm CH stretch
ν_7	3168.10	b_u	quartets asymm CH stretch
ν_{10}	3160.65	b_u	duos asymm CH stretch
ν_{11}	3156.72	b_u	non-bay edges asymm CH stretch
ν_{13}	1650.92	a_g	edge symm CC stretch
ν_{14}	1648.71	b_u	terminal rings CC stretch
ν_{15}	1638.32	a_g	edge asymm CC stretch
ν_{16}	1629.01	b_u	outer “naphthalene” edge symm CC stretch
ν_{17}	1599.42	a_g	ring fusing carbons CC stretch
ν_{18}	1553.44	a_g	duos/quartets asymm bay CH bend
ν_{19}	1549.78	b_u	terminal edge CC stretch
ν_{20}	1514.52	b_u	duos/quartets symm bay CH bend
ν_{21}	1480.80	a_g	duos/quartets symm bay CH bend
ν_{22}	1458.74	a_g	duos/quartets asymm bay CH bend
ν_{23}	1458.58	b_u	duos/quartets asymm bay CH bend
ν_{24}	1451.54	b_u	quartets asymm CH bend

Table 4.8 Mode descriptions and harmonic frequencies [cm^{-1}] of the IR active modes and modes involved in IR active combination bands/resonances identified in the CH–stretching region of chrysene.

ID	sym	exp[26]	rel. I[26]	anharm	rel. I	components	I sources
a	b_u	3110.7	0.29	-	-	-	
b	b_u	3107.4	0.54	3120.9	0.49	ν_2	ν_2
						$\nu_{16} + \nu_{18}$	
						$\nu_{13} + \nu_{20}$	
c	b_u	3102.3	0.40	3106.2	0.74	ν_2	ν_2
						$\nu_{13} + \nu_{20}$	
d	b_u	3095.7	0.65	3098.7	1	ν_6	ν_2
						$\nu_{15} + \nu_{20}$	ν_6
e	b_u	3091.0	0.23	3092.9	0.51	$\nu_{17} + \nu_{19}$	ν_2
							ν_3
							ν_7
f	b_u	3078.4	0.78	3084.3	0.70	$\nu_{14} + \nu_{21}$	ν_2
							ν_6
g	b_u	3073.8	0.93	3069.7	0.78	ν_6	ν_6
						$\nu_{14} + \nu_{21}$	
h	b_u	3070.5	0.71	3067.0	0.57	ν_{11}	ν_6
						$\nu_{13} + \nu_{23}$	ν_7
						$\nu_{14} + \nu_{22}$	
i	b_u	3063.0	1	3063.6	0.66	$\nu_{16} + \nu_{21}$	ν_6
							ν_7
j	b_u	3058.8	0.56	3058.7	0.59	$\nu_{15} + \nu_{23}$	ν_3, ν_7
k	b_u	3053.7	0.75	3057.0	0.63	ν_{10}	ν_7
						$\nu_{17} + \nu_{20}$	ν_{10}
						$\nu_{14} + \nu_{22}$	
	b_u					$\nu_{15} + \nu_{23}$	ν_7
l	b_u	3049.0	0.45	3050.6	0.44	$\nu_{14} + \nu_{22}$	ν_2
						$\nu_{13} + \nu_{23}$	
						$\nu_{18} + \nu_{19}$	
						$\nu_{17} + \nu_{20}$	
	b_u					$\nu_{17} + \nu_{20}$	ν_2
							ν_6
							ν_{10}
m	b_u	3043.5	0.32	3044.9	0.53	$\nu_{13} + \nu_{24}$	ν_2
							ν_6
n	b_u	3035.1	0.50	3039.7	0.69	ν_7	ν_7
						$\nu_{15} + \nu_{24}$	
o	b_u	3020.3	0.50	3024.4	0.86	ν_6	ν_6
						ν_{11}	
						$\nu_{18} + \nu_{20}$	
						$\nu_{15} + \nu_{24}$	
p	b_u	3010.1	0.20	3012.8	0.33	ν_{10}	ν_{10}
						ν_{11}	
						$\nu_{17} + \nu_{23}$	
						$\nu_{13} + \nu_{24}$	

Table 4.9 Line positions [cm^{-1}], relative intensities, dominant resonant components, and origin of intensities for the bands of the chrysene in the high–resolution gas–phase IR absorption spectra obtained in a molecular beam (this work) and the theoretical anharmonic spectrum (this work) as shown in figure 4.13.

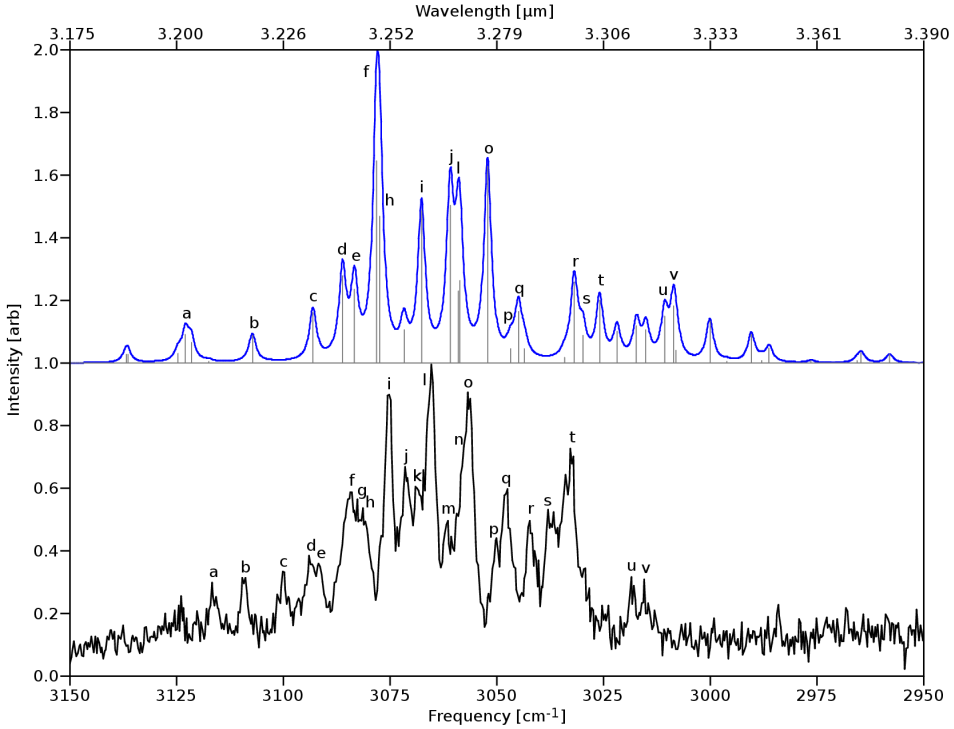

Figure 4.14 Anharmonic QFF IR spectrum of phenanthrene (this work) compared to high–resolution gas–phase IR absorption spectra obtained in a molecular beam (this work).

Mode	Freq	Symm	Description
ν_1	3199.53	a_1	bay symm CH stretch
ν_2	3189.22	b_2	quartets/bay asymm CH stretch
ν_4	3179.79	b_2	quartets/bay asymm CH stretch
ν_5	3172.54	a_1	duo symm CH stretch
ν_6	3168.11	a_1	quartets/duo symm CH stretch
ν_8	3157.11	b_2	quartets/duo asymm CH stretch
ν_9	3156.72	a_1	quartets (no bay) asymm stretch
ν_{11}	1651.44	a_1	corner edge CC stretch
ν_{12}	1646.57	b_2	terminal edge CC stretch
ν_{13}	1634.92	a_1	full edge CC stretch
ν_{14}	1601.29	b_2	ring fusing carbons CC stretch
ν_{15}	1556.72	a_1	quartets/asymm bay CH bend
ν_{16}	1529.25	b_2	quartets/duo/symm bay CH bend
ν_{17}	1486.53	b_2	quartets/duo/symm bay CH bend
ν_{18}	1466.74	a_1	quartets/duo/symm bay CH bend
ν_{19}	1446.12	a_1	quartets/asymm bay CH bend
ν_{20}	1442.79	b_2	duo/quartet (no bay) CH bend

Table 4.10 Mode descriptions and harmonic frequencies [cm^{-1}] of the IR active modes and modes involved in IR active combination bands/resonances identified in the CH–stretching region of phenanthrene.

ID	sym	exp[26]	rel. I[26]	anharm	rel. I	components	I sources
a	a_1	3116.6	0.24	3122.9	0.13	$\nu_{12}+\nu_{16}$	ν_1
						$\nu_{13}+\nu_{15}$	
	b_2					$\nu_{11}+\nu_{16}$	ν_4
b	b_2	3109.6	0.25	3107.4	0.10	$\nu_{13}+\nu_{16}$	ν_2
c	b_2	3100.0	0.28	3093.1	0.18	ν_2	ν_2
						ν_7	
						$\nu_{14}+\nu_{15}$	
d	a_1	3094.0	0.33	3086.2	0.33	ν_1	ν_1
						ν_3	
						$\nu_{12}+\nu_{17}$	
						$\nu_{12}+\nu_{16}$	
e	b_2	3091.8	0.30	3083.4	0.31	ν_4	ν_4
						$\nu_{11}+\nu_{17}$	
						$\nu_{13}+\nu_{16}$	
f	b_2	3084.3	0.55	3078.0	1	ν_2	ν_2
						ν_4	ν_4
						$\nu_{11}+\nu_{17}$	
g	-	3082.8	0.53	-	-	-	-
h	a_1	3081.5	0.50	3076.7	0.60	ν_1	ν_1
						ν_3	
						$2\nu_{15}$	
i	b_2	3075.4	0.89	3067.7	0.53	ν_2	ν_2
						$\nu_{13}+\nu_{17}$	ν_4
j	a_1	3071.6	0.64	3060.9	0.63	ν_5	ν_5
						$\nu_{14}+\nu_{16}$	
						$\nu_{11}+\nu_{18}$	
						$\nu_{11}+\nu_{19}$	
k	-	3069.0	0.57	-	-	-	-
l	b_2	3065.3	1	3059.0	0.59	ν_8	ν_4
						ν_4	ν_2
						$\nu_{13}+\nu_{17}$	
						$\nu_{12}+\nu_{18}$	
	a_1					ν_3	ν_6
						ν_6	
m	-	3061.8	0.05	-	-	-	-
n	-	3057.0	0.90	-	-	-	-
o	a_1	3056.4	0.88	3052.2	0.66	ν_5	ν_5
						ν_6	ν_6
						$\nu_{14}+\nu_{16}$	
p	b_2	3050.3	0.40	3046.8	0.12	ν_8	ν_8
						$\nu_{12}+\nu_{19}$	
q	a_1	3047.9	0.55	3045.0	0.21	ν_9	ν_9
						$\nu_{12}+\nu_{20}$	
r	a_1	3042.4	0.45	3031.9	0.30	ν_5	ν_5
						$2\nu_{15}$	
						$\nu_{11}+\nu_{18}$	
s	a_1	3037.6	0.47	3030.2	0.16	$2\nu_{15}$	ν_5
						$\nu_{14}+\nu_{17}$	
t	b_2	3032.8	0.68	3026.0	0.23	ν_4	ν_4
						$\nu_{12}+\nu_{18}$	
u	a_1	3018.6	0.26	3010.6	0.20	ν_6	ν_6
						$\nu_{14}+\nu_{17}$	
						$\nu_{13}+\nu_{19}$	
v	b_2	3015.5	0.25	3008.7	0.25	ν_4	ν_4
						ν_8	
						$\nu_{12}+\nu_{19}$	
						$\nu_{13}+\nu_{20}$	

Table 4.11 Line positions [cm^{-1}], relative intensities, dominant resonant components, and origin of intensities for the bands of the phenanthrene in the high–resolution gas–phase IR absorption spectra obtained in a molecular beam (this work) and the theoretical anharmonic spectrum (this work) as shown in figure 4.14.

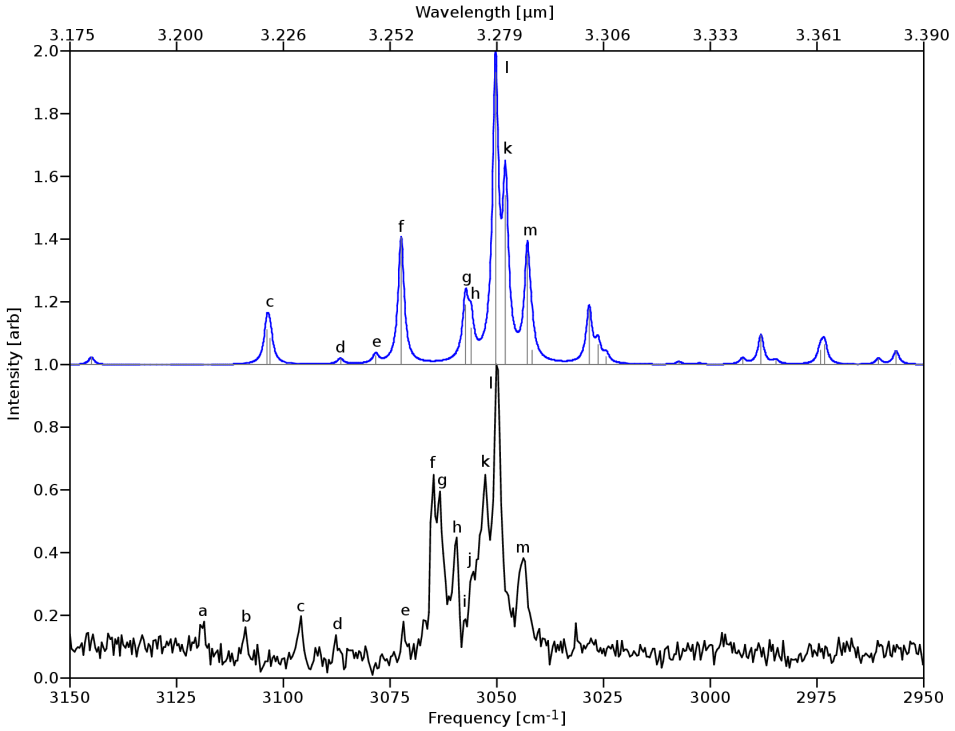

Figure 4.15 Anharmonic QFF IR spectrum of pyrene (this work) compared to high–resolution gas–phase IR absorption spectra obtained in a molecular beam (this work).

Mode	Freq	Symm	Description
ν_2	3181.48	b_{1u}	trios symm CH stretch
ν_4	3172.18	b_{2u}	duos symm CH stretch
ν_6	3164.47	b_{2u}	trios (no middle CH) asymm CH stretch
ν_{10}	3153.84	b_{1u}	duos assym CH stretch
ν_{11}	1660.92	a_g	middle “naphthalene” CC stretch
ν_{12}	1635.58	b_{2u}	edge asymm CC stretch
ν_{13}	1626.43	b_{1u}	terminal “benzene” symm CC stretch
ν_{14}	1618.23	b_{3g}	terminal “benzene” asymm CC stretch
ν_{16}	1528.64	b_{3g}	trios/duos symm CH bend
ν_{17}	1508.36	b_{2u}	trios/duos asymm CH bend
ν_{18}	1478.71	b_{1u}	duos symm CH bend
ν_{19}	1456.19	b_{1u}	trios/duos assym CH bend
ν_{20}	1453.29	b_{2u}	trios symm CH bend

Table 4.12 Mode descriptions and harmonic frequencies [cm^{-1}] of the IR active modes and modes involved in IR active combination bands/resonances identified in the CH–stretching region of pyrene.

ID	sym	exp[26]	rel. I[26]	anharm	rel. I	components	I sources
a	-	3118.7	0.12	-	-	-	-
b	-	3108.9	0.10	-	-	-	-
c	b_{1u}	3096.0	0.12	3103.7	0.17	$\nu_{12} + \nu_{16}$	ν_2
	b_{2u}					$\nu_{11} + \nu_{17}$	ν_4
d	b_{2u}	3087.8	0.08	3086.7	0.02	$\nu_{13} + \nu_{16}$	ν_6
e	b_{1u}	3071.9	0.11	3078.4	0.04	$\nu_{11} + \nu_{18}$	ν_2
							ν_{10}
f	b_{1u}	3064.9	0.59	3072.5	0.41	ν_2	ν_2
						$\nu_{14} + \nu_{17}$	
g	b_{2u}	3063.3	0.56	3057.3	0.24	ν_6	ν_4
						$\nu_{11} + \nu_{20}$	ν_6
h	b_{1u}	3059.5	0.39	3056.5	0.21	$\nu_{11} + \nu_{19}$	ν_2
i	-	3057.5	0.13	-	-	-	-
j	-	3055.6	0.29	-	-	-	-
k	b_{2u}	3052.9	0.60	3048.1	0.65	ν_4	ν_4
						ν_6	
l	b_{1u}	3049.8	1	3050.4	1	ν_2	ν_2
m	b_{2u}	3044.0	0.34	3042.9	0.40	ν_6	ν_4
						$\nu_{11} + \nu_{20}$	ν_6

Table 4.13 Line positions [cm^{-1}], relative intensities, dominant resonant components, and origin of intensities for the bands of the pyrene in the high–resolution gas–phase IR absorption spectra obtained in a molecular beam (this work) and the theoretical anharmonic spectrum (this work) as shown in figure 4.15.

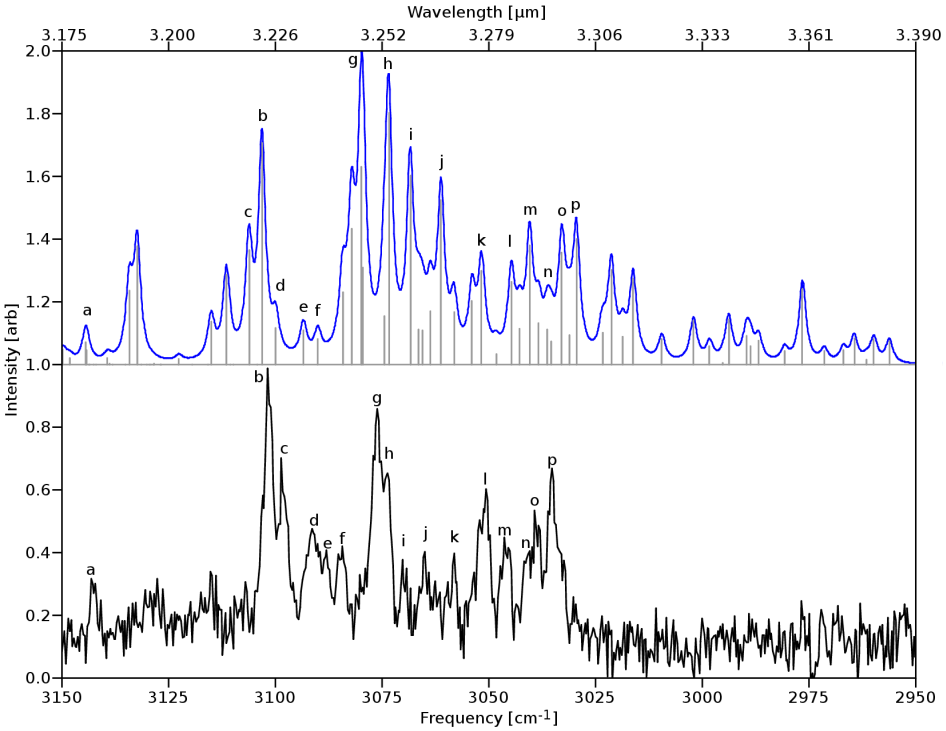

Figure 4.16 Anharmonic QFF IR spectrum of triphenylene (this work) compared to high–resolution gas–phase IR absorption spectra obtained in a molecular beam (this work).

Mode	Freq	Symm	Description
ν_1	3213.85		bay symm CH stretch
ν_2	3211.89	e	bay symm CH stretch
ν_3	3211.39	e	bay symm CH stretch
ν_4	3196.22	e	quartet/bay asymm CH stretch
ν_5	3195.83	e	quartet/bay asymm CH stretch
ν_6	3192.73		bay asymm CH stretch
ν_7	3181.62		quartet symm (no bay) CH stretch
ν_8	3178.58	e	quartet/bay asymm CH stretch
ν_9	3178.52	e	quartet/bay asymm CH stretch
ν_{12}	3164.34		quartet/bay asymm CH stretch
ν_{13}	1644.06		edge CC stretch
ν_{14}	1639.66	e	edge CC stretch
ν_{15}	1639.55	e	edge CC stretch
ν_{16}	1610.63	e	ring fusing carbons CC stretch
ν_{17}	1610.43	e	ring fusing carbons CC stretch
ν_{18}	1580.25		quartets/bay asymm CH bend
ν_{19}	1527.60	e	two symm bay/one asymm bay CH bend
ν_{20}	1526.99	e	one symm bay/two asymm bay CH bend
ν_{21}	1486.15		quartet (no bay) symm CH bend
ν_{22}	1474.23		three asymm bay CH bends
ν_{23}	1462.40	e	quartets/bay symm CH bend
ν_{24}	1462.17	e	quartets/bay symm CH bend

Table 4.14 Mode descriptions and harmonic frequencies [cm^{-1}] of the IR active modes and modes involved in IR active combination bands/resonances identified in the CH–stretching region of triphenylene. Due to the symmetry lowering of triphenylene the symmetries for each mode are not given. However, modes that are degenerate under $\mathcal{D}_{3h}$ symmetry are indicated by the symbol "e".

ID	exp[26]	rel. I[26]	anharm	rel. I	components	I sources
a	3143.2	0.20	3144.5	0.13	$2\nu_{16}$	ν_2
					$2\nu_{17}$	ν_8
					$\nu_{15} + \nu_{18}$	ν_9
b	3101.8	1	3103.2	0.77	$\nu_{15} + \nu_{20}$	ν_3
					ν_3	
c	3098.7	0.68	3106.3	0.40	$\nu_1\ \nu_5$	ν_2
					$\nu_{13} + \nu_{20}$	ν_3
d	3091.5	0.43	3100.0	0.13	$\nu_{14} + \nu_{20}$	ν_2
						ν_9
e	3088.1	0.35	3093.5	0.12	$\nu_{17} + \nu_{20}$	ν_8
					$\nu_{16} + \nu_{20}$	ν_9
f	3084.3	0.36	3090.2	0.09	ν_7	ν_8
					$\nu_{16} + \nu_{20}$	ν_9
					$\nu_{17} + \nu_{20}$	
g	3076.2	0.85	3079.8	1	ν_5	ν_2
					$2\nu_{18}$	ν_8
					ν_7	ν_9
					ν_2	
					ν_9	
					ν_8	
					$\nu_{13} + \nu_{19}$	
h	3073.8	0.62	3073.7	0.96	ν_3	ν_3
					ν_6	
					ν_4	
					$\nu_{14} + \nu_{19}$	
i	3070.3	0.31	3068.5	0.64	ν_2	ν_2
					ν_5	
					ν_4	
					ν_1	
j	3065.0	0.34	3061.3	0.57	ν_9	ν_9
					$2\nu_{18}$	
k	3058.2	0.34	3051.8	0.33	$\nu_{18} + \nu_{20}$	ν_3
l	3050.8	0.57	3044.8	0.29	$\nu_{16} + \nu_{24}$	ν_2
					$\nu_{16} + \nu_{22}$	ν_9
					$\nu_{17} + \nu_{22}$	
m	3046.4	0.40	3040.5	0.41	ν_8	ν_8
					$\nu_{17} + \nu_{19}$	
					$\nu_{15} + \nu_{21}$	
n	3040.6	0.35	3036.1	0.17	ν_7	ν_9
					$2\nu_{20}$	
					$\nu_{14} + \nu_{16}$	
					$\nu_{16} + \nu_{22}$	
					$\nu_{14} + \nu_{21}$	
					$\nu_{13} + \nu_{23}$	
					$\nu_{17} + \nu_{21}$	
					$\nu_{16} + \nu_{24}$	
o	3039.4	0.50	3032.9	0.40	ν_9	ν_9
					$\nu_{16} + \nu_{21}$	
					$\nu_{13} + \nu_{23}$	
					$\nu_{16} + \nu_{19}$	
p	3035.3	0.64	3029.7	0.45	ν_8	ν_8
					ν_{12}	
					$\nu_{18} + \nu_{20}$	

Table 4.15 Line positions [cm^{-1}], relative intensities, dominant resonant components, and origin of intensities for the bands of the triphenylene in the high–resolution gas–phase IR absorption spectra obtained in a molecular beam (this work) and the theoretical anharmonic spectrum (this work) as shown in figure 4.16.